arXiv:2505.23282v1 [cond-mat.str-el] 29 May 2025

Tuning the Chern number of Kitaev quantum spin liquid

Seong Jun Kwon,[1,2] Kyusung Hwang,[3,*] and Suk Bum Chung[2,4,†]

[1] *Department of Applied Physics, The University of Tokyo, Bunkyo, Tokyo 113-8656, Japan*
[2] *Department of Physics and Natural Science Research Institute, University of Seoul, Seoul 02504, Republic of Korea*
[3] *Department of Applied Physics, Kyung Hee University, Yongin 17104, Republic of Korea*
[4] *School of Physics, Korea Institute for Advanced Study, Seoul 02455, Republic of Korea*

(Dated: August 16, 2025)

It is now well understood that non-Kitaev spin interactions can be added to the Kitaev quantum spin liquid by applying external fields. Recent years have seen intensive discussion on the possible phase transitions that these spin interactions induce. In this paper, we will show through the perturbation theory the possibility of accessing a gapped spin liquid phase with a higher Chern number through, in contrast to the cases studied in literature, a continuous phase transition. Such a transition may be induced by external tuning parameters such as electric field and hydrostatic pressure.

I. INTRODUCTION

One of the most notable developments in quantum magnetism has been the proposal by Kitaev of the exactly soluble model of quantum spin liquid [1]. The study of quantum spin liquids (QSLs)—exotic and elusive phases of matter that are electrically insulating and magnetically disordered yet involve many-body quantum entanglement [2–5]—has repeatedly encountered difficulties even on the theoretical level in determining the stability of the quantum spin liquid ground state. The Kitaev honeycomb model offers manifest clarity on this issue thanks to the exact solutions of the Kitaev spin liquid (KSL) ground state and its fractionalized quasiparticle excitations, Majorana fermions. With the realization that transition metal atoms with strong spin-orbit coupling can approximate the Kitaev honeycomb model [6, 7], the Kitaev magnetism became a subject of intensive experimental investigations as well [8–11]. Remarkably, experimental signatures of the KSL and Majorana fermions have been reported by the recent measurements of thermal Hall effect and heat capacity on the Kitaev material α-$RuCl_3$ [12–15].

Extensive literature on the stability of the KSL phase has arisen in recent years owing, on one hand, to the existence of candidate materials and, on the other hand, to the issue being much better defined on microscopic levels than any other quantum spin liquid models. In all candidate materials, physics of the transition metal atoms, essential for the bond-dependent spin interaction, never completely turns off the non-Kitaev spin interaction [6, 7, 16, 17], and these non-Kitaev interactions tend to favor magnetically ordered states over the KSL phase [16, 18–25]. Furthermore, recent years have seen various studies on the additional *tunable* non-Kitaev spin interactions induced by an external electric field [26–31] or hydrostatic pressure [23, 32–39].

That the non-Kitaev spin interactions can destabilize the KSL phase raises the possibility of its driving a continuous phase transition to topologically distinct quantum spin liquid phases. The transitions to a non-KSL phase driven by the non-Kitaev interactions investigated so far have been of the first-order, and all of them have been between the KSL and a spin-ordered and topologically trivial states, therefore involving both the change in topology and the breaking of spin rotational symmetry. On the other hand, starting with the Haldane honeycomb model [40], it has been recognized that a continuous phase transition is possible when change in topology occurs without any symmetry breaking. Investigations of continuous phase transitions in the Kitaev materials have so far concentrated mainly on the transition between the KSL phases with the opposite chirality [1, 30, 41]. Meanwhile, recent variational Monte Carlo calculations [24, 25] have found a topologically non-trivial quantum spin liquid phase with a higher winding number (a 'proximate KSL') stabilized by sufficiently strong non-Kitaev spin interactions, but the direct transition from the KSL to the proximate KSL have been found to be of the first order, *i.e.* discontinuous. A proximate KSL topologically distinct from the KSL yet with a continuous transition from KSL would be more convenient to identify experimentally, especially if this continuous transition can be accessed through external tuning parameters. While one type of non-Kitaev spin interaction was shown to induce a continuous transition from the KSL to a proximate KSL state [42], it has not been accompanied by discussion on symmetry-allowed tuning of non-Kitaev interaction terms.

In this paper, we investigate possible continuous transitions from the KSL to proximate KSLs by the non-Kitaev spin interactions that are tunable with external electric and magnetic fields and hydrostatic pressure. By performing a perturbative analysis, we find that with a weak but finite magnetic field along the (111) direction, the increasing electric field along the (111) direction or hydrostatic pressure can lead to the continuous topologi-

* kyusung.hwang@khu.ac.kr
† sbchung0@uos.ac.kr

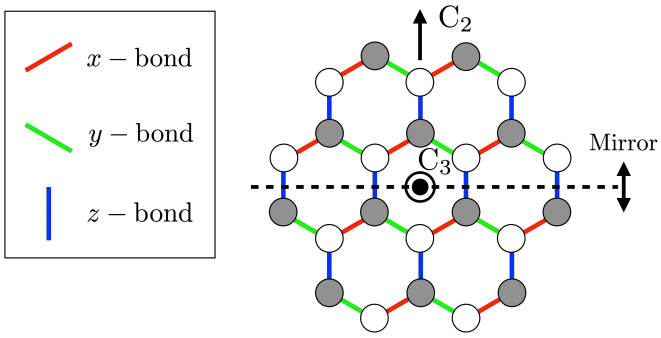


FIG. 1: Lattice symmetries of the Kitaev Honeycomb model. Three types of bonds of the Kitaev model are denoted by three different colors: x-bond (red), y-bond (green), and z-bond (blue). A and B sublattices of the honeycomb lattice are indicated by gray and white circles, respectively. The Kitaev model has the C_3 rotation symmetry about the normal axis to each hexagon plaquette, the C_2 rotation symmetry about the axis of each bond, and the mirror reflection symmetry with respect to the normal plane bisecting each bond (dashed line).

cal transition from the non-Abelian KSL with the Chern number of ± 1 to the proximate Abelian KSL with the Chern number of ∓ 2 [1, 24, 25, 42, 43]. At zero magnetic field, we identify a variety of interesting nodal structures in the excitation spectrum including (i) multiple Majorana cones, (ii) Majorana quadratic band touching, and (iii) Majorana line node. We analyze how magnetic fields gap out the zero-field nodal structures, leading to the KSLs with nonzero Chern numbers. Interestingly, certain types of nodal structures survive under magnetic fields in the form of gap closing at the topological transition between the distinct KSLs with different Chern numbers. We remark on implications of our results in quantum information applications of the KSL [44, 45].

The paper is organized as follows. In Sec. II, we present our model Hamiltonian and discuss its symmetry with and without external tuning; this discussion will make clear how some of the non-Kitaev interactions can be externally tuned. By requiring our external tuning parameters, *e.g.* electric field, magnetic field, and hydrostatic pressure, to all respect the C_3 rotational symmetry around the (111) direction, our analysis is simplified, with the number of independent spin interaction parameters restricted. In Sec. III, we present our perturbative analysis on the non-Kitaev terms in the zero-flux sector, focusing on how effective longer-range Majorana hoppings arise along with their impacts on the topological structure of the KSL and the resulting topological transitions. Lastly, we present discussion our results, including implications on quantum information applications of the KSL in Sec. IV. Details of the perturbation theory and the topological transitions are provided in Appendices.

II. MODEL HAMILTONIAN AND SYMMETRY

We consider a generalized Kitaev model which contains various non-Kitaev interactions including Dzyaloshinskii-Moriya (DM) and Γ' interactions and Zeeman coupling. Our model Hamiltonian takes the form,

$$H = \sum_{\langle jk\rangle_\gamma} \boldsymbol{\sigma}_j \cdot \mathbf{M}_\gamma \cdot \boldsymbol{\sigma}_k - \mathbf{h} \cdot \sum_j \boldsymbol{\sigma}_j, \tag{1}$$

where $\boldsymbol{\sigma}_j = (\sigma_j^x, \sigma_j^y, \sigma_j^z)$ is the three-component vector of the Pauli matrices operating on the spin-1/2 at site j. The 3×3 matrix $\mathbf{M}_\gamma$ describes exchange interactions of nearest-neighboring spins at γ-bonds, where $\gamma \in \{x, y, z\}$ (Fig. 1). To be specific, the matrix at z-bonds is given by

$$\mathbf{M}_z = \mathbf{M}_K + \mathbf{M}_{\Gamma'} + \mathbf{M}_D, \tag{2}$$

$$\mathbf{M}_K = \begin{pmatrix} 0 & 0 & 0 \\ 0 & 0 & 0 \\ 0 & 0 & K \end{pmatrix}$$

$$\mathbf{M}_{\Gamma'} = \begin{pmatrix} 0 & 0 & \Gamma' \\ 0 & 0 & \Gamma' \\ \Gamma' & \Gamma' & 0 \end{pmatrix}$$

$$\mathbf{M}_D = \begin{pmatrix} 0 & D_2 & -D_1 \\ -D_2 & 0 & D_1 \\ D_1 & -D_1 & 0 \end{pmatrix}$$

i.e., Kitaev, Γ', and DM interactions. The other matrices $\mathbf{M}_{x,y}$ for x, y-bonds can be obtained by cyclic permutations of $\mathbf{M}_z$ (equivalently C_3 rotations of the z-bond interaction term). In a vector representation, the DM interactions can be represented by

$$\mathbf{D}_\gamma \cdot (\boldsymbol{\sigma}_j \times \boldsymbol{\sigma}_k), \tag{4}$$

with the bond-dependent DM vectors,

$$\mathbf{D}_x = (D_2, D_1, D_1) \quad \text{for } x\text{−bond}, \tag{5}$$
$$\mathbf{D}_y = (D_1, D_2, D_1) \quad \text{for } y\text{−bond}, \tag{6}$$
$$\mathbf{D}_z = (D_1, D_1, D_2) \quad \text{for } z\text{−bond}. \tag{7}$$

In this representation, we choose the convention that site j is on the A sublattice and site k is on the B sublattice. The last term of H represents the Zeeman coupling with a magnetic field along the out-of-plane direction,

$$\mathbf{h} = \frac{h}{\sqrt{3}}(1, 1, 1). \tag{8}$$

Among the symmetries of the pure Kitaev model, our model preserves the C_3 rotational symmetry around the normal axis, *i.e.* the (111) direction, to each plaquette (see Table I).

Table I also makes it clear that, among the cases where the hydrostatic pressure, the applied external electric

Symmetry	K	Γ'	$D_{1,2}$	$\mathbf{h} \parallel (111)$
C_3 rotation	✓	✓	✓	✓
C_2 rotation	✓	✓		
Time reversal	✓	✓	✓	
Spatial inversion	✓	✓		✓
Mirror reflection	✓	✓	✓	

TABLE I: Preserved symmetries by each interaction of the model Hamiltonian H [Eq. (1)]. See Fig. 1 for the definitions of the C_3 rotation, C_2 rotation, and Mirror reflection.

Zeeman-type	Every site	σ_j^x, σ_j^y, σ_j^z
D_2-type	x-bond	$\sigma_j^y\sigma_k^z$, $\sigma_j^z\sigma_k^y$
	y-bond	$\sigma_j^z\sigma_k^x$, $\sigma_j^x\sigma_k^z$
	z-bond	$\sigma_j^x\sigma_k^y$, $\sigma_j^y\sigma_k^x$
D_1/Γ'-type	x-bond	$\sigma_j^x\sigma_k^y$, $\sigma_j^y\sigma_k^x$, $\sigma_j^x\sigma_k^z$, $\sigma_j^z\sigma_k^x$
	y-bond	$\sigma_j^y\sigma_k^z$, $\sigma_j^z\sigma_k^y$, $\sigma_j^y\sigma_k^x$, $\sigma_j^x\sigma_k^y$
	z-bond	$\sigma_j^z\sigma_k^x$, $\sigma_j^x\sigma_k^z$, $\sigma_j^z\sigma_k^y$, $\sigma_j^y\sigma_k^z$

TABLE II: Classification of the non-Kitaev terms based on flux-creation patterns.

field, and the applied magnetic field are all present, our model possesses the highest symmetry possible. To begin with, the Γ' terms represent the simplest spin interaction arising from the trigonal distortion for the spin-1/2 model on the honeycomb lattice with the edge-sharing octahedron structure; it preserves not only the C_3 rotational symmetry but all the symmetries of the Kitaev terms. It has been reported [23, 28, 32, 34, 41] that such trigonal distortion term can be induced by applying hydrostatic pressure. Secondly, while any non-zero DM interactions would break both the C_2 rotational symmetry around each bond axis and the spatial inversion exchanging the two sublattices of the honeycomb lattice, our model does preserve the C_3 rotational symmetry. Such DM interaction can be induced by applying a uniform electric field along the (111) direction, in which case there remains the mirror symmetry with respect to the planes perpendicularly bisecting each bond. This mirror symmetry leaves us with the two independent coefficients for the DM interactions (D_1 and D_2) as shown in Eq. (2), each proportional to the magnitude of the applied electric field [16, 28–30]. Lastly, any non-zero Zeeman field $\mathbf{h}$ will break the time-reversal symmetry preserved by all the spin interactions represented by the first term of Eq. (1), but $\mathbf{h} \parallel (111)$ leaves the C_3 rotational symmetry intact. The discussion on how the DM and Γ' spin interactions arise from combination of electron hoppings and electronic interactions is presented in Appendix A.

III. PERTURBATION ANALYSIS AND TOPOLOGICAL TRANSITION

We investigate influence of the non-Kitaev interactions on the Kitaev spin liquid state of the pure Kitaev model via a perturbation theory. To this end, the Hamiltonian is separated into two parts:

$$H = H_0 + H_1, \tag{9}$$

where H_0 is the pure Kitaev model

$$H_0 \equiv K \sum_{\langle jk\rangle_\gamma} \sigma_j^\gamma \sigma_k^\gamma$$

and H_1 contains the non-Kitaev interactions (D_1, D_2, Γ', h) which are going to be considered as perturbations. By performing a perturbative analysis with the non-Kitaev term, we find effective multi-spin interactions that lead to topological transitions in the Kitaev spin liquid.

A. Perturbation Theory of the Extended Kitaev Model

Discussion of the pure Kitaev model (H_0) is a prerequisite to present any perturbation theory. Two properties of H_0 are of particular interest. One is its commutation with the flux operator of any unit hexagon plaquette p defined as [1]

$$W_p = \prod_{\langle jk\rangle_\gamma \in p} \sigma_j^\gamma \sigma_k^\gamma; \tag{10}$$

note that the plaquette flux operator also commutes with each other, $[W_p, W_{p'}] = 0$. The other is that through a Majorana representation of spin-1/2 operators, the most symmetric form being [1]

$$\sigma_j^\gamma = i b_j^\gamma c_j, \tag{11}$$

where b_j^γ and c_j are Majorana fermions, it can be written as the Hamiltonian where the nearest-neighbor hopping of the c-Majorana fermions is coupled to a $\mathbb{Z}_2$ gauge field,

$$H_0 = -iK \sum_{\langle jk\rangle_\gamma} (i b_j^\gamma b_k^\gamma) c_j c_k. \tag{12}$$

These two properties are intimately related as W_p turns out to be nothing more than the $\mathbb{Z}_2$ gauge flux, *i.e.*

$$W_p = \prod_{\langle A,B\rangle_\gamma \in p} (i b_A^\gamma b_B^\gamma), \tag{13}$$

where A, B are the sublattice labels as shown in Figs. 2, 3, and 4. Lastly, it has been shown that the H_0 ground state is in the zero flux sector, *i.e.* $W_p = +1$ for all plaquettes.

As our analysis perturbatively treats H_1 to obtain the effective Hamiltonian in the zero-flux sector, a natural starting point would be to study how the terms of H_1 affect the plaquette flux W_p. As we shall show here, no

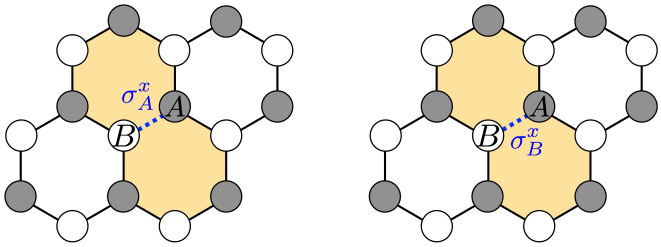


FIG. 2: Flux creation by Zeeman-type terms at x-bond: σ^x_A (left) and σ^x_B (right). In each case, yellow plaquettes indicate $\mathbb{Z}_2$ fluxes created by the spin operator. The blue dashed line marks the sign-changed $\mathbb{Z}_2$ gauge field by the spin operator ($ib^x_A b^x_B : \ +1 \rightleftarrows -1$).

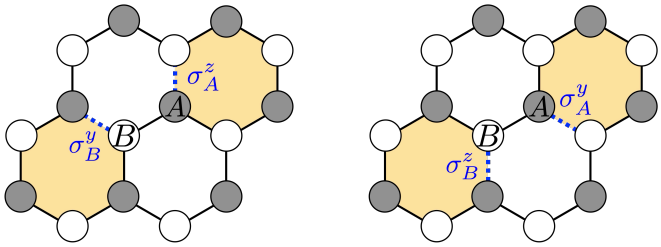


FIG. 3: Flux creation by D_2-type terms at x-bond: $\sigma^z_A\sigma^y_B$ (left) and $\sigma^y_A\sigma^z_B$ (right). The blue dashed line again marks the sign-changed $\mathbb{Z}_2$ gauge field.

term in the H_1 leaves W_p invariant. The underlying reason is that σ^γ_j induces a $\mathbb{Z}_2$-flux pair in adjacent hexagons with a γ-bond coming in between, as depicted in Fig. 2 [1, 41]; this can be seen from Eqs. (11) and (13). It should be obvious that this is directly applicable to the linear spin terms of the Zeeman Hamiltonian $H_Z = -\mathbf{h}\cdot\sum_j \sigma_j$.

But the quadratic spin terms of H_1 also generate $\mathbb{Z}_2$-flux pairs, albeit of different types; the quadratic terms are classified into two types, D_2-type and D_1/Γ'-type (Table II). Flux patterns created by these quadratic terms are illustrated in Figs. 3, 4

It can be seen clearly now that in the zero flux sector, all the first-order perturbation terms should vanish and the second-order terms are the lowest order terms after H_0, resulting in the effective zero-flux sector Hamiltonian of [1, 29, 30, 33, 41, 42].

$$H_{\rm eff} = P_0\left(H_0 - \sum_m \frac{H_1|m\rangle\langle m|H_1}{\Delta_m}\cdots\right)P_0, \tag{14}$$

where $|m\rangle$ is the intermediate state with a $\mathbb{Z}_2$-flux pair, Δ_m is the energy cost for creating the $\mathbb{Z}_2$-flux pair, and P_0 is the projection operator that projects to the zero-flux sector:

$$P_0 = \prod_p \frac{1+W_p}{2}. \tag{15}$$

we have established above that there are actually only two different values for Δ_m's, $\Delta \approx 0.2672|K|$ for the first-neighbor $\mathbb{Z}_2$-flux pair of Figs. 2, 4 and $\Delta' \approx 0.2372|K|$ for the second-neighbor $\mathbb{Z}_2$-flux pair of Fig. 3 [1]. The non-vanishing second-order perturbation terms obtained from Eq. (14) should consist of two-, three-, four-spin interaction terms, up to the projection onto the zero-flux sector, obtained from the product of a pair of terms from H_1 that preserves all $\mathbb{Z}_2$ flux W_p. The resulting $H_{\rm eff}$ would be in the form of

$$H_{\rm eff} = P_0\left(K_1\sum_{\langle jk\rangle_\gamma}\sigma^\gamma_j\sigma^\gamma_k + K_2\sum_{\langle jkl\rangle_{\alpha\beta}}\sigma^\alpha_j\sigma^\gamma_k\sigma^\beta_l + \sum_{\langle jklm\rangle_{\alpha\gamma\beta}}K_3^{\alpha\beta\gamma}\sigma^\alpha_j\sigma^\beta_k\sigma^\alpha_l\sigma^\beta_m + K_4\sum_{\langle jklm\rangle_{\alpha\beta\alpha}}\sigma^\alpha_j\sigma^\gamma_k\sigma^\gamma_l\sigma^\alpha_m\right)P_0, \tag{16}$$

where $\langle jkl\cdots\rangle_{\alpha\gamma\cdots}$ denotes consecutive sites connected by the α-bond between sites j,k, the γ-bond between sites k,l *etc*, and the three Greek indices are all different from each other ($\alpha\neq\beta\neq\gamma$). The effective spin interactions appearing in $H_{\rm eff}$ are essentially products of Kitaev bond interactions as they are the only terms that can survive under the projection operator P_0;

$$\sigma^\alpha_j\sigma^\gamma_k\sigma^\beta_l \propto (\sigma^\alpha_j\sigma^\alpha_k)(\sigma^\beta_k\sigma^\beta_l),$$

$$\sigma^\alpha_j\sigma^\beta_k\sigma^\alpha_l\sigma^\beta_m \propto (\sigma^\alpha_j\sigma^\alpha_k)(\sigma^\gamma_k\sigma^\gamma_l)(\sigma^\beta_l\sigma^\beta_m),$$

$$\sigma^\alpha_j\sigma^\gamma_k\sigma^\gamma_l\sigma^\alpha_m \propto (\sigma^\alpha_j\sigma^\alpha_k)(\sigma^\beta_k\sigma^\beta_l)(\sigma^\alpha_l\sigma^\alpha_m).$$

See Fig. 5 for a visualization of the effective spin interactions. We will later show that the spin interaction parameters come out to be

$$K_1 = K - \frac{2h^2}{3\Delta} + \frac{2D_2^2}{\Delta'}, \tag{17}$$

$$K_2 = \frac{4h\Gamma'}{\sqrt{3}\Delta}, \tag{18}$$

$$K_3^{\alpha\beta\gamma} = -\frac{2\left(\Gamma' + \varepsilon_{\alpha\beta\gamma}D_1\right)^2}{\Delta}, \tag{19}$$

$$K_4 = \frac{2(D_1^2 - \Gamma'^2)}{\Delta}, \tag{20}$$

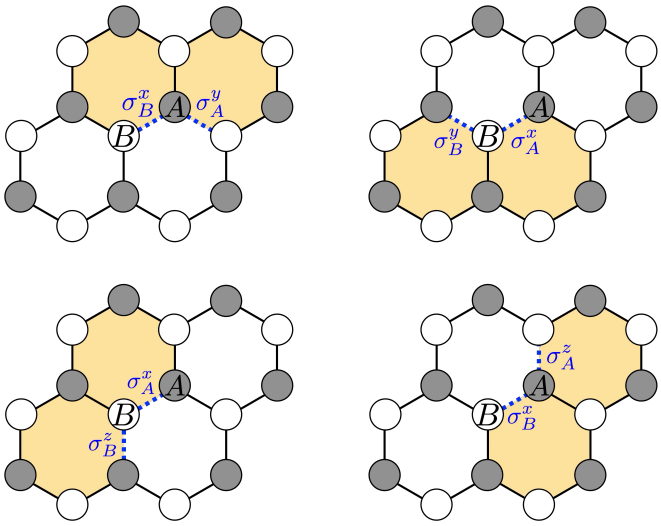


FIG. 4: Flux creation by D_1/Γ'-type terms at x-bond: $\sigma_A^y\sigma_B^x$ (top left), $\sigma_A^x\sigma_B^y$ (top right), $\sigma_A^x\sigma_B^z$ (bottom left), and $\sigma_A^z\sigma_B^x$ (bottom right).

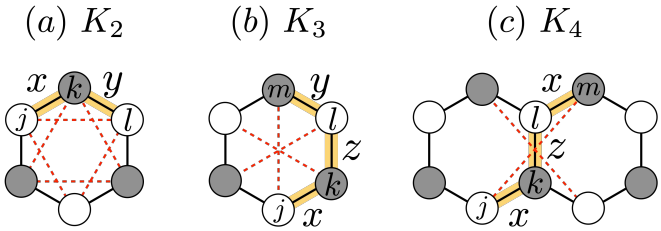


FIG. 5: Illustration of the effective multi-spin interactions of H_{eff} [Eq. (16)]. (a) K_2 term on two consecutive Kitaev bonds $\langle jkl\rangle_{xy}$. (b) K_3 term on three consecutive Kitaev bonds $\langle jklm\rangle_{xzy}$. (c) K_4 term on three consecutive Kitaev bonds $\langle jklm\rangle_{xzx}$. The red dashed lines depict the additional hopping paths of Majorana fermions resulting from the multi-spin interactions.

where $\varepsilon_{\alpha\beta\gamma}$ is the antisymmetric Levi-Civita tensor.

But H_{eff} can also be expressed as the hopping of Majorana fermions of the range varying from the nearest neighbor to the fourth neighbor [29, 33, 42, 46]. This implies that the third- and fourth-neighbor hopping is of the same order of magnitude as the second-neighbor hopping. Given that study of an analogous model based on graphene and the Haldane model have found topological phase transitions [42, 47], we shall now proceed to derive each non-vanishing second-order perturbation term.

1. 2- and 3-Spin Interactions

We shall first discuss how to derive the first two terms of Eq. (16). It would be relatively less complicated to follow in the sense that only 2 or 3 spins are involved. However, these terms do not represent the qualitatively more important part of our results; for the reasons discussed below, they do not drive the topological phase transitions.

We have stated through Eq. (16) that among the second-order perturbation terms, some are of the same form as H_0; they are hence of the lesser importance qualitatively. These terms can be attributed to two different sources. One comes from products of two Zeeman-type terms, or h^2-terms, that preserve the $\mathbb{Z}_2$-flux [1]:

$$\begin{aligned} H_{\text{ZZ}} &= -\frac{1}{\Delta}P_0\left[-h\sum_j\left(\frac{1}{\sqrt{3}}\sigma_j^x+\frac{1}{\sqrt{3}}\sigma_j^y+\frac{1}{\sqrt{3}}\sigma_j^z\right)\right]^2 P_0 \\ &= -\frac{2h^2}{3\Delta}\sum_{\langle A,B\rangle_\gamma} P_0\sigma_A^\gamma\sigma_B^\gamma P_0. \end{aligned} \tag{21}$$

The other comes from products of two D_2-type terms, for the derivation of which we can first consider only on the x-bond

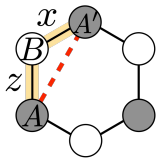
$$\begin{aligned} H^x_{D_2D_2} =& -\frac{1}{\Delta'}\sum_{\langle A,B\rangle_x} P_0\left[D_2\left(\sigma_A^y\sigma_B^z-\sigma_A^z\sigma_B^y\right)\right]^2 P_0 \\ =& \frac{D_2^2}{\Delta'}\sum_{\langle A,B\rangle_x} P_0\left(\sigma_A^y\sigma_B^z\sigma_A^z\sigma_B^y+\sigma_A^z\sigma_B^y\sigma_A^y\sigma_B^z\right)P_0 \\ =& \frac{2D_2^2}{\Delta'}\sum_{\langle A,B\rangle_x} P_0\sigma_A^x\sigma_B^x P_0. \end{aligned}$$

By repeating for the y,z-bonds, we can obtain

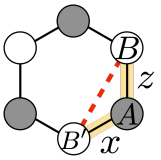
$$H_{D_2D_2} = \sum_{\alpha\in\{x,y,z\}} H^\alpha_{D_2D_2} = \frac{2D_2^2}{\Delta'}\sum_{\langle A,B\rangle_\alpha} P_0\sigma_A^\alpha\sigma_B^\alpha P_0, \tag{22}$$

which completes our derivation of $K_1 = K - \frac{2h^2}{3\Delta} + \frac{2D_2^2}{\Delta'}$ in Eq. (16)

The next term in Eq. (16) is the 3-spin interaction whose parameter K_2 as we shall show is nonzero only for $h\neq 0$. It is obtained at the second order of perturbation in our model as products of a single Zeeman-type term with a single D_1/Γ'-type term that preserve the $\mathbb{Z}_2$-flux. As a concrete example, we derive the 3-spin interactions in the following two cases.



$$\langle ABA'\rangle_{zx}: \quad \begin{aligned} &\tfrac{2}{\Delta}P_0\left[\tfrac{h}{\sqrt{3}}\sigma_A^z\right]\left[(\Gamma'+D_1)\sigma_B^y\sigma_{A'}^x\right]P_0+\tfrac{2}{\Delta}P_0\left[(\Gamma'-D_1)\sigma_A^z\sigma_B^y\right]\left[\tfrac{h}{\sqrt{3}}\sigma_{A'}^x\right]P_0\\ &=\tfrac{4h\Gamma'}{\sqrt{3}\Delta}P_0\sigma_A^z\sigma_B^y\sigma_{A'}^xP_0. \end{aligned} \tag{23}$$



$$\langle BAB'\rangle_{zx}: \quad \begin{aligned} &\tfrac{2}{\Delta}P_0\left[(\Gamma'+D_1)\sigma_B^z\sigma_A^y\right]\left[\tfrac{h}{\sqrt{3}}\sigma_{B'}^x\right]P_0+\tfrac{2}{\Delta}P_0\left[\tfrac{h}{\sqrt{3}}\sigma_B^z\right]\left[(\Gamma'-D_1)\sigma_A^y\sigma_{B'}^x\right]P_0\\ &=\tfrac{4h\Gamma'}{\sqrt{3}\Delta}P_0\sigma_B^z\sigma_A^y\sigma_{B'}^xP_0. \end{aligned} \tag{24}$$

By applying lattice translations and C_3 rotations to the two cases, we can generate all the 3-spin interactions and eventually obtain the whole 3-spin term:

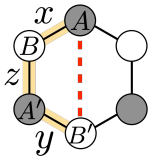
$$H_{\text{eff}}^{(2)}=\frac{4h\Gamma'}{\sqrt{3}\Delta}\sum_{\langle jkl\rangle_{\alpha\beta}}P_0\sigma_j^\alpha\sigma_k^\gamma\sigma_l^\beta P_0, \tag{25}$$

completing our derivation of $K_2=\frac{4h\Gamma'}{\sqrt{3}\Delta}$ in Eq. (16). With the regards the magnitude of the 3-spin interaction, we will focus on the small Zeeman field regime, *i.e.* $|h|\ll|D_1|,|\Gamma'|$, and hence it will not be as large as that of the 4-spin interaction which we will derive next. Nonetheless, we shall later show how this 3-spin interaction can not be ignored for any $h\Gamma'\neq 0$.

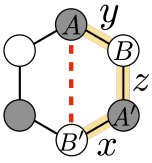
2. 4-Spin Interactions

We can now show that the principal effect of the second-order perturbation arises from the induced 4-spin interaction terms. This is because the terms with the parameters quadratic in D_1 and Γ' contribute only to the 4-spin interaction parameters $K_3^{\alpha\beta\gamma}$ and K_4 in Eq. (16).

The 4-spin term with the parameter $K_3^{\alpha\beta\gamma}$ can be obtained by second-order perturbation on the following types of three consecutive bonds:



$$\langle ABA'B'\rangle_{xzy}: \quad \begin{aligned} &-\tfrac{2}{\Delta}P_0\left[(\Gamma'+D_1)\,\sigma_A^x\sigma_B^y\right]\left[(\Gamma'+D_1)\,\sigma_{A'}^x\sigma_{B'}^y\right]P_0\\ &=-\tfrac{2\left(\Gamma'+D_1\right)^2}{\Delta}P_0\sigma_A^x\sigma_B^y\sigma_{A'}^x\sigma_{B'}^yP_0, \end{aligned} \tag{26}$$



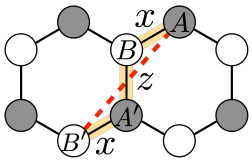
$$\langle ABA'B'\rangle_{yzx}: \quad \begin{aligned} &-\tfrac{2}{\Delta}P_0\left[(\Gamma'-D_1)\,\sigma_A^y\sigma_B^x\right]\left[(\Gamma'-D_1)\,\sigma_{A'}^y\sigma_{B'}^x\right]P_0\\ &=-\tfrac{2\left(\Gamma'-D_1\right)^2}{\Delta}P_0\sigma_A^y\sigma_B^x\sigma_{A'}^y\sigma_{B'}^xP_0. \end{aligned} \tag{27}$$

Note that the two different paths connecting the same end points (A and B') lead to different results, which are manifestations of the C_2 rotation symmetry as shown in Fig. 1 broken by the DM interactions as stated in Tab. I. Collecting all the 4-spin interactions related by lattice translations and C_3 rotations, we obtain the whole 4-spin term of this type

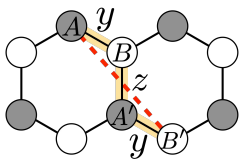
$$H_{\text{eff}}^{(3)}=-\sum_{\langle jklm\rangle_{\alpha\gamma\beta}}\frac{2\left(\Gamma'+\varepsilon_{\alpha\beta\gamma}D_1\right)^2}{\Delta}P_0\sigma_j^\alpha\sigma_k^\beta\sigma_l^\alpha\sigma_m^\beta P_0, \tag{28}$$

where we again take the convention that j and l sites belong to the A sublattice but k and m sites belong to the B sublattice; this completes our derivation of $K_3^{\alpha\beta\gamma}=-\frac{2(\Gamma'+\varepsilon_{\alpha\beta\gamma}D_1)^2}{\Delta}$ in Eq. (16).

The 4-spin term with the parameter K_4 can also be computed in the similar fashion. Here we consider the following three consecutive bonds:



$$\langle ABA'B'\rangle_{xzx}: \quad \begin{array}{l} -\frac{2}{\Delta}P_0\left[(\Gamma'+D_1)\sigma_A^x\sigma_B^y\right]\left[(\Gamma'-D_1)\sigma_{A'}^y\sigma_{B'}^x\right]P_0 \\ =-\frac{2(\Gamma'^2-D_1^2)}{\Delta}P_0\sigma_A^x\sigma_B^y\sigma_{A'}^y\sigma_{B'}^xP_0. \end{array} \tag{29}$$



$$\langle ABA'B'\rangle_{yzy}: \quad \begin{array}{l} -\frac{2}{\Delta}P_0\left[(\Gamma'-D_1)\sigma_A^y\sigma_B^x\right]\left[(\Gamma'+D_1)\sigma_{A'}^x\sigma_{B'}^y\right]P_0 \\ =-\frac{2(\Gamma'^2-D_1^2)}{\Delta}P_0\sigma_A^y\sigma_B^x\sigma_{A'}^x\sigma_{B'}^yP_0. \end{array} \tag{30}$$

Interestingly, these two cases give identical results since they are related by the mirror symmetry that is still preserved by the DM interactions. Because of this property, the whole 4-spin term this type does not possess any particular bond dependence:

$$H_{\rm eff}^{(4)}=\frac{2\left(D_1^2-\Gamma'^2\right)}{\Delta}\sum_{\langle jklm\rangle_{\alpha\beta\alpha}}P_0\sigma_j^\alpha\sigma_k^\gamma\sigma_l^\gamma\sigma_m^\alpha P_0, \tag{31}$$

where we take j and l sites from the same sublattice but k and m sites from the other sublattice; this completes our derivation of $K_4=\frac{2(D_1^2-\Gamma'^2)}{\Delta}$ in Eq. (16).

B. Topology analysis from Majorana Hamiltonian

As our main purpose is to analyze the topological characteristics of $H_{\rm eff}$ [Eq. (16)], which can be carried out simplest from the Majorana fermion representation in the momentum space, the logical next step is to obtain its Majorana fermion representation in the real space, where the 3- and 4-spin interactions can be expressed as longer-ranged Majorana hoppings. We note that in the Majorana representation the zero-flux projection operator P_0 can be taken care of through the gauge fixing

$$ib_A^\gamma b_B^\gamma=+1$$

when A, B are nearest-neighbor sites belonging to the A- and B-sublattice, respectively; this sets $W_p=+1$ for all plaquettes from the Eq. (13) Majorana representation $W_p=\prod_{\langle A,B\rangle_\gamma}(ib_A^\gamma b_B^\gamma)$. Applying this gauge fixing and the Eq. (11) Majorana representation of spin-1/2 operators, $\sigma_j^\gamma=ib_j^\gamma c_j$ after re-writing all the spin interaction of $H_{\rm eff}$ as products of the Kitaev spin interaction, we obtain

$$H_{\rm eff}=-iK_1\sum_{\langle A,B\rangle_1}c_Ac_B-iK_2\left(\sum_{\langle A,A'\rangle_2}c_Ac_{A'}+\sum_{\langle B,B'\rangle_2}c_Bc_{B'}\right)+i\left(K_3^{xyz}+K_3^{yxz}\right)\sum_{\langle A,B\rangle_3}c_Ac_B-iK_4\sum_{\langle A,B\rangle_4}c_Ac_B, \tag{32}$$

where $\langle A,B\rangle_n$ denotes the n-th neighbor A, B belonging to the A-, B-sublattice respectively and $\langle A(B),A'(B')\rangle_2$ denotes the 2nd neighbor pairs both belonging to the A(B)-sublattice in the counter-clockwise direction.

Next we transform the above real-space Hamiltonian of Eq. (32) into the momentum-space Hamiltonian. We first note that the first term of Eq. (32) is a Majorana fermion analogue of the nearest-neighbor hopping only graphene model. Hence, the Majorana cones (MCs) are present at the K and K′ points in the first Brillouin zone, analogous to the Dirac cones of graphene [1, 10]. We have seen that the electric field induced DM interaction and the trigonal distortion induced Γ' interaction effectively give rise to additional distant hopping terms through the perturbative treatment of off-diagonal spin interactions [29, 33]. This system therefore resembles graphene with distant-neighbor hopping [47]. To show this, we first define the Fourier transformation of the Majorana fermion as

$$c_{\mathbf{r},\rho}=\frac{1}{\sqrt{N}}\sum_{\mathbf{k}}e^{i\mathbf{k}\cdot\mathbf{r}}c_{\mathbf{k},\rho} \tag{33}$$

where $\mathbf{r}$ is the position vector of lattice site, $\rho(\in A,B)$ denotes the sublattice, and $\mathbf{k}$ is crystal momentum. The lattice vectors $\{\mathbf{d}_m^{(n)}\}$ connecting n-th neighboring sites associated with the $K_n(n=1,2,3,4)$ interaction terms are depicted in Fig. 6. By applying the Fourier transfor-

mation, the entire Hamiltonian can be expressed as

$$H_{\text{eff}} = \frac{1}{2}\sum_{\mathbf{k}} \begin{pmatrix} c_{-\mathbf{k},A} & c_{-\mathbf{k},B} \end{pmatrix} \begin{pmatrix} M(\mathbf{k}) & f(\mathbf{k}) \\ f^*(\mathbf{k}) & -M(\mathbf{k}) \end{pmatrix} \begin{pmatrix} c_{\mathbf{k},A} \\ c_{\mathbf{k},B} \end{pmatrix} \tag{34}$$

where $f(\mathbf{k}) \equiv f_1(\mathbf{k}) + f_3(\mathbf{k}) + f_4(\mathbf{k})$ with

$$f_1(\mathbf{k}) = -iK_1 \sum_{m=1}^{3} e^{-i\mathbf{k}\cdot\mathbf{d}_m^{(1)}}, \tag{35}$$

$$f_3(\mathbf{k}) = i\left(K_3^{xyz} + K_3^{yxz}\right) \sum_{m=1}^{3} e^{-i\mathbf{k}\cdot\mathbf{d}_m^{(3)}}, \tag{36}$$

$$f_4(\mathbf{k}) = -iK_4 \sum_{m=1}^{6} e^{-i\mathbf{k}\cdot\mathbf{d}_m^{(4)}}, \tag{37}$$

and

$$M(\mathbf{k}) = -K_2 \sum_{m=1}^{3} \sin\left[\mathbf{k}\cdot\mathbf{d}_m^{(2)}\right]. \tag{38}$$

Note that the Majorana mass term $M(\mathbf{k})$ becomes nonzero only in presence of a magnetic field [Eq. (18)]. The Majorana Hamiltonian H_{eff} [Eq. (34)] gives the energy dispersion of Majorana fermion:

$$\epsilon(\mathbf{k}) = \pm\sqrt{|f(\mathbf{k})|^2 + M^2(\mathbf{k})}. \tag{39}$$

We shall first consider the $h = 0$ case and then move on to the $h \neq 0$ case.

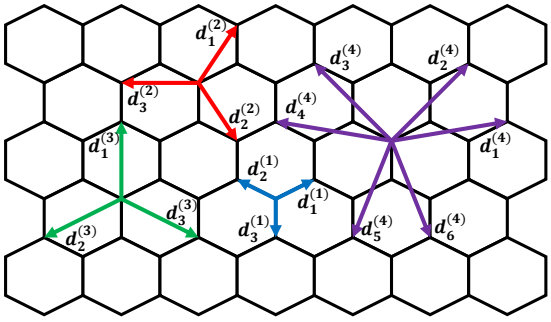


FIG. 6: The lattice vectors are defined as follows: $\mathbf{d}_m^{(1)}$, represented by a blue arrow, is the nearest-neighbor lattice vector. $\mathbf{d}_m^{(2)}$, represented by a red arrow, is the second-neighbor lattice vector. $\mathbf{d}_m^{(3)}$, represented by a green arrow, is the third-neighbor lattice vector. $\mathbf{d}_m^{(4)}$, represented by a purple arrow, is the fourth-neighbor lattice vector.

1. *Additional Majorana cones for $h = 0$*

The $h = 0$ case is closely analogous to the graphene with the long-range hopping, which implies, for strong enough third- and the fourth-neighbor hopping [42, 47, 48], the possibility of additional Majorana cones (AMCs). For this case, the effective Hamiltonian of Eq. (34) can be represented by the matrix

$$\begin{pmatrix} 0 & f(\mathbf{k}) \\ f^*(\mathbf{k}) & 0 \end{pmatrix} = \boldsymbol{\mathcal{F}}(\mathbf{k})\cdot\boldsymbol{\sigma}, \tag{40}$$

where $\boldsymbol{\mathcal{F}}(\mathbf{k}) = [\text{Re}f(\mathbf{k}), -\text{Im}f(\mathbf{k}), 0]$ and $\boldsymbol{\sigma} = [\sigma_x, \sigma_y, \sigma_z]$ ($\sigma_{x,y,z}$ are the Pauli spin matrices). AMCs can be identified by solving the equation of $f(\mathbf{k}) = 0$; more explicitly,

$$\sum_{m=1}^{3} e^{-i\mathbf{k}\cdot\mathbf{d}_m^{(1)}} + 2\zeta \sum_{m=1}^{3} e^{-i\mathbf{k}\cdot\mathbf{d}_m^{(3)}} + \eta \sum_{m=1}^{6} e^{-i\mathbf{k}\cdot\mathbf{d}_m^{(4)}} = 0, \tag{41}$$

where the two parameters,

$$\zeta = -\frac{K_3^{xyz} + K_3^{yxz}}{2K_1} = \frac{2\left(D_1^2 + \Gamma'^2\right)/\Delta}{K + 2D_2^2/\Delta'}, \tag{42}$$

$$\eta = \frac{K_4}{K_1} = \frac{2\left(D_1^2 - \Gamma'^2\right)/\Delta}{K + 2D_2^2/\Delta'}, \tag{43}$$

determine the number of AMCs and their topological structures. Note our perturbation theory gives us $\zeta/\eta = (D_1^2 + \Gamma'^2)/(D_1^2 - \Gamma'^2)$, and hence $|\zeta| \geq |\eta|$.

Any AMCs that arise are located on the 3 high-symmetry lines of the 1st BZ joining Γ, K, M, and K′. This can be shown analytically for $\zeta \to \pm\infty$ or $\eta \to \pm\infty$ cases [47]. The latter is particularly simple, as one can read off $\sum_{m=1}^{3} \exp\left[-i\mathbf{k}\cdot\mathbf{d}_m^{(3)}\right] = \sum_{m=1}^{3} \exp\left[i2\mathbf{k}\cdot\mathbf{d}_m^{(1)}\right]$ from Fig. 6; this implies that the midpoints of the ΓK and ΓK′ lines are additional solutions for $\sum_{m=1}^{3} \exp\left[-i\mathbf{k}\cdot\mathbf{d}_m^{(3)}\right] = 0$. Fig. 8 shows some characteristic examples of how the AMCs thus arises around K. Given that $k_y = 0$ for one such high-symmetry line, it would be sufficient to solve Eq. (41) just for $\mathbf{k} = k_x\hat{\mathbf{x}}$, which gives us

$$(2x+1)[1 + 2\zeta(2x-1) + 2\eta(2x^2-1)] = 0, \tag{44}$$

where $x \equiv \cos\frac{\sqrt{3}}{2}k_x$. An obvious solution of the above equation is

$$x_{\text{K}} = -1/2, \tag{45}$$

corresponding to the original MC at the K point. There can be two more solutions,

$$x_\pm = \frac{-\zeta \pm \sqrt{\zeta^2 - \eta(1 - 2\zeta - 2\eta)}}{2\eta}, \tag{46}$$

provided that the two conditions, $x_\pm \in \mathbb{R}$ and $|x_\pm| \leq 1$, are satisfied. The explicit constraints on

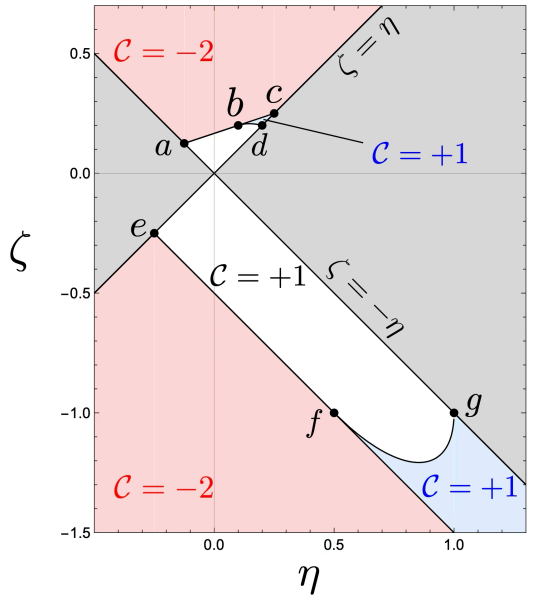


FIG. 7: Phase diagram of the Majorana Hamiltonian [Eq. (32)] in the parameter space of (η, ζ). The colored regions represent the number of zero-field Majorana cones or the number of solutions of Eq. (44): (i) 7 MCs near the K valley or $\{x_{\rm K}, x_+, x_-\}$ (blue), (ii) 4 MCs near the K valley or $\{x_{\rm K}, x_+\}/\{x_{\rm K}, x_-\}$ (red), and (iii) a single MC near the K valley or $\{x_{\rm K}\}$ (white). The gray region is excluded from our consideration due to the condition, $|\zeta| \geq |\eta|$, deduced from our perturbation theory. The applied magnetic field gaps out the zero-field MCs in each case, resulting in the nonzero Chern number: (i) $\mathcal{C}=+1$ (blue), (ii) $\mathcal{C}=-2$ (red), and (iii) $\mathcal{C}=+1$ (white). The marked points are: $a=(-1/8, 1/8)$, $b=(1/10, 1/5)$, $c=(1/4, 1/4)$, $d=(1/5, 1/5)$, $e=(-1/4, -1/4)$, $f=(1/2, -1)$, and $g=(1, -1)$. The explicit expressions of the boundary lines are provided in Eqs. (D1), (D2), and (D3) of Appendix D. Along the boundary lines, the zero-field system exhibits nontrivial Majorana band topology such as quadratic band touching and line node (discussed in Figs. 9, 10, 11, and 12). The chirality structures of the zero-field MCs are illustrated in Fig. 8.

ζ and η due to the two conditions are provided in Eqs. (D1), (D2), and (D3) of Appendix D. Depending on the parameter values of ζ and η, the solution of Eq. (44) corresponds to one of the three cases: (i) $\{x_{\rm K}, x_+, x_-\}$, (ii) $\{x_{\rm K}, x_+\}$ or $\{x_{\rm K}, x_-\}$, and (iii) $\{x_{\rm K}\}$ (Fig. 7).

Although we have focused on AMCs along the ΓK line, there exist two more lines related to the ΓK line by threefold rotation symmetry about the K point. Hence, x_+ (and also x_-) actually gives a trio of AMCs related by the threefold rotation (see Fig. 8). It must be remembered that the K′ point should also have the same structure of AMCs due to time reversal symmetry.

Each MC should not only have zero energy but also possess a well-defined chirality, which means the winding number of the vector $\boldsymbol{\mathcal{F}}(\mathbf{k})$ around the zero-energy point [43, 47]. The chirality of each MC is given by

$$\chi = \mathrm{sgn}\left[\frac{1}{2\pi}\hat{\mathbf{z}}\cdot\int_{\rm MC} d^2\mathbf{k}\left\{\frac{\partial\hat{\boldsymbol{\mathcal{F}}}(\mathbf{k})}{\partial k_x}\times\frac{\partial\hat{\boldsymbol{\mathcal{F}}}(\mathbf{k})}{\partial k_y}\right\}\right], \quad (47)$$

where the 2D integration is performed over only single MC. It is straightforward to obtain the latter from the first derivative of $\boldsymbol{\mathcal{F}}(\mathbf{k})$, which is required to be non-vanishing at an MC. Calculating this first derivative is further simplified for $k_y = 0$ as that will give us $\partial_{k_x}\mathcal{F}_x = \partial_{k_y}\mathcal{F}_y = 0$, and Eq. (47) simplifies to

$$\chi = -\mathrm{sgn}[(\partial_{k_x}\mathcal{F}_y)(\partial_{k_y}\mathcal{F}_x)]. \quad (48)$$

From the chirality calculations, we obtain the following features of the topological structure of AMCs:

- In the K-valley, the chiralities of the MCs are determined by

$$\chi(x_{\rm K}) = +1, \quad (49)$$
$$\chi(x_\pm) = \mp\mathrm{sgn}(\zeta-\eta) = \mp\mathrm{sgn}(\zeta). \quad (50)$$

  In the last equality, we applied the property, $|\zeta| \geq |\eta|$. A trio of AMCs corresponding to x_+ (or x_-) share the same chirality. However, the trio of x_+'s and the other trio of x_-'s have the opposite signs of chiralities.

- The chiralities of MCs in the K′-valley are opposite to those of the corresponding MCs in the K-valley.

- Majorana quadratic band touching can arise when the trio of x_+-AMCs with $\chi(x_+) = -1$ merge into the original K point MC with $\chi(x_{\rm K}) = +1$. Their merger leads to a Majorana quadratic band touching with the Berry phase of -2π [47, 49]. This actually occurs when $\zeta = (1-\eta)/4$.

- The net chirality in the K-valley is either ± 1 or ∓ 2 (Fig. 8).

- The Majorana line node is generated in the special case of $\zeta = \eta$ (e.g., by setting $\Gamma' = 0$). In this case, the line node

$$4\eta\cos^2\frac{\sqrt{3}k_x}{2} + 4\eta\cos\frac{\sqrt{3}k_x}{2}\cos\frac{3k_y}{2} + 1 = 4\eta, \quad (51)$$

  appears in place of AMCs for $\eta > \frac{1}{5}$ or $\eta < -\frac{1}{4}$ [47]; it forms a closed loop around the Γ point for $\eta < -\frac{1}{4}$ or $\eta > \frac{1}{4}$ and around the K and K′ points for $\frac{1}{5} < \eta < \frac{1}{4}$, as can be seen from Fig. 12. We note that its 3D analogue has been discussed for the Kitaev model on the hyperhoneycomb lattice [50].

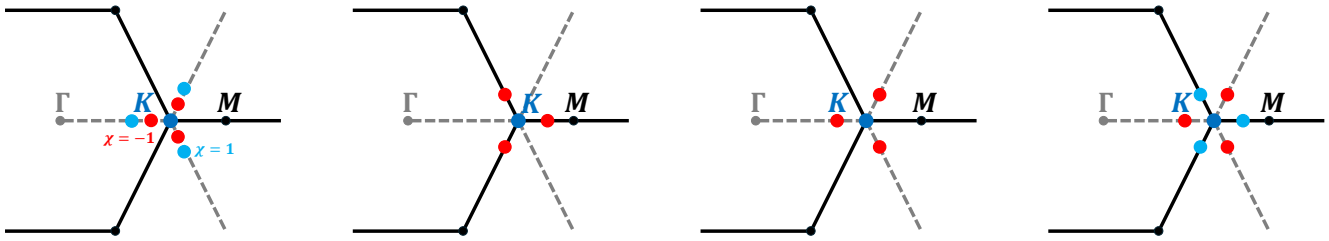


FIG. 8: Some characteristic AMC distribution near the K point. The dark blue dot represents the MC at K-point with the positive chirality. Light blue(red) dots represent AMCs with the positive(negative) chirality. We take $M(\mathbf{k}) > 0$ in the K valley. (a) The case of $\zeta < -1$ in the $D_1 = 0$ limit has the Chern number $C = +1$. (b) The case of $\frac{1}{8} < \zeta < \frac{1}{3}$ in the $D_1 = 0$ limit has the Chern number $C = -2$. (c) The case of $\zeta > \frac{1}{3}$ in the $D_1 = 0$ limit and $\zeta < -\frac{1}{4} - \frac{\delta}{8}$ or $\zeta > \frac{1}{4} - \frac{\delta}{8}$ in the $\Gamma' \ll |D_1|$ limit has the Chern number $C = -2$. (d) The case of $\frac{1}{5} + \frac{\delta}{25} < \zeta < \frac{1}{4} - \frac{\delta}{8}$ in the $\Gamma' \ll |D_1|$ limit has the Chern number $C = +1$.

2. *Topological characteristics for $h \neq 0$*

Associated with the emergence of AMCs for $h = 0$ is the continuous topological quantum phase transition for $h \neq 0$ between the gapped non-Abelian KSL with the Chern number ± 1 and the gapped Abelian proximate KSL with the Chern number ∓ 2 [1, 24, 25, 42, 43]. Both phases are gapped out by the Zeeman-induced term of Eq. (38): $M(\mathbf{k}) = -\frac{4\Gamma' h}{\sqrt{3}\Delta} \sum_{m=1}^{3} \sin\left[\mathbf{k} \cdot \mathbf{d}_m^{(2)}\right]$. Given that the effective Majorana Hamiltonian matrix of Eq. (40) can now be written as $\boldsymbol{\mathcal{F}} \cdot \boldsymbol{\sigma}$ where the direction of $\boldsymbol{\mathcal{F}} = (\mathrm{Re}f, -\mathrm{Im}f, M)$ is well-defined, the Chern number can be obtained from the familiar formula

$$\mathcal{C} = \frac{1}{4\pi} \int_{\mathrm{BZ}} d^2\mathbf{k} \hat{\boldsymbol{\mathcal{F}}} \cdot \left(\frac{\partial \hat{\boldsymbol{\mathcal{F}}}}{\partial k_x} \times \frac{\partial \hat{\boldsymbol{\mathcal{F}}}}{\partial k_y} \right).$$

However, for most cases with small h, $\mathcal{C}$ arises entirely from MCs gapped by $M(\mathbf{k})$, in which cases the above Chern number formula reduces to the summation over all i-th MCs, *i.e.*

$$\mathcal{C} = \frac{1}{2} \sum_i \chi_i \mathrm{sgn}(M_i), \tag{52}$$

where χ_i and M_i are the chirality and the mass term $M(\mathbf{k})$ evaluated at the i-th MC, respectively [47]. One key point in evaluating this simpler Chern number formula is that $M(\mathbf{k})$ vanishes only along the ΓM lines and its sign is constant within a valley but opposite between the two valleys, resulting in $\mathcal{C} \neq 0$ from the sets of MCs with opposite chiralities between the two valleys [1, 29, 40, 41]. We have seen from Fig. 8 that for $h = 0$ the AMCs of the same chirality always appear in trios in the same valley, and this can be considered the underlying reason for the emergence of the proximate KSL phase with $|\mathcal{C}| > 1$ for $h \neq 0$. By applying Eq. (52) on Fig. 7, we obtain $\mathcal{C} = \mp 2$ for the red domains and $\mathcal{C} = \pm 1$ elsewhere. Below we will discuss three examples, showing the types and chiralities of the AMCs for $h = 0$ along with their locations and the resulting $\mathcal{C}$ when $h \neq 0$ gives $M_{\mathrm{K}} > 0$ (see Fig. 8 for the illustration). We will also show that the transition between the $\mathcal{C} = \pm 1$ KSL and the $\mathcal{C} = \mp 2$ proximate KSL is continuous in the sense that it is always accompanied by a gap closing at the transition point, and that the gap closing occurs either at the three M points with an MC appearing at each (for which $\zeta = \frac{1}{6} + \frac{1}{3}\eta$ or ac line in Fig. 7) or at the Γ point with the Majorana quadratic band touching (QBT) (for which $\zeta = -\eta - \frac{1}{2}$ or ef line in Fig. 7); see Appendix E for details. We emphasize that it is $M(\mathbf{k})$ that determines the gap closing point characteristics: three MCs at the three M points or a Majorana QBT at the Γ point.

- Our first example is the case with no electric field, *i.e.* D_1=0 or $\zeta = -\eta$. Fig. 9 visualizes the topological quantum phase transition occurring in this case. Details of the change of band topology over four distinct states are discussed below.

$D_1 = 0$ limit ($\zeta = -\eta$)			
ζ	AMCs	χ	$\mathcal{C}$
$\zeta < -1$	$x_+ \in [\Gamma, \mathrm{K}]$	$+1$	$+1$
	$x_- \in [\Gamma, \mathrm{K}]$	-1	
$-1 < \zeta < \frac{1}{8}$	None		$+1$
$\frac{1}{8} < \zeta < \frac{1}{3}$	$x_+ \in [\mathrm{M}, \mathrm{K}]$	-1	-2
	x_- doesn't exist		
$\zeta > \frac{1}{3}$	$x_+ \in [\Gamma, \mathrm{K}]$	-1	-2
	x_- doesn't exist		

The energy gap closes only once at $\zeta = \frac{1}{8}$, at which the appearance of an MC at each of the three M points signifies a continuous $\Delta\mathcal{C} = 3$ topological phase transition. Conversely the gap does not close when $\Delta\mathcal{C} = 0$ even when there is a change in AMCs for $h = 0$. One such case occurs at $\zeta = \frac{1}{3}$ where all AMCs may merge to K and K′ for $h = 0$, but this means that $h \neq 0$ gaps out a

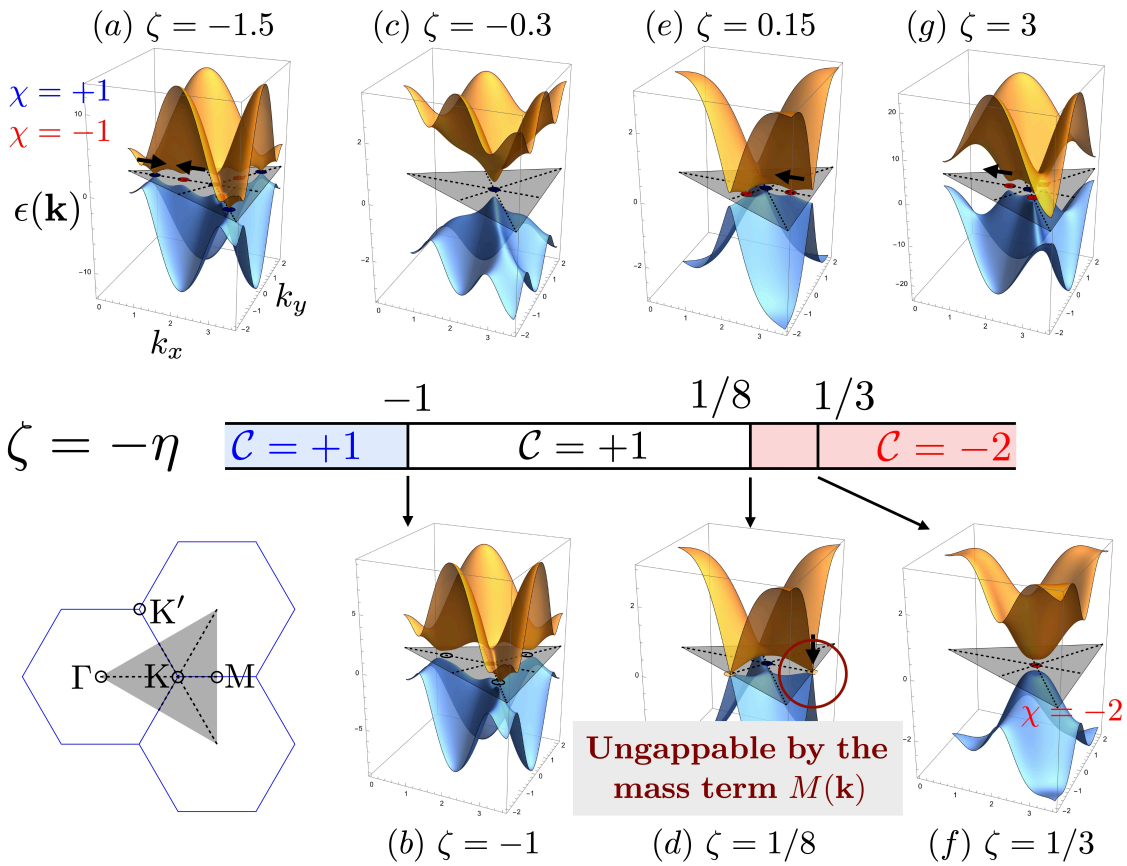


FIG. 9: Topological quantum phase transition on the $\zeta = -\eta$ line of Fig. 7 in presence of a magnetic field ($h \neq 0$). In the parameter space of $\zeta(= -\eta)$, the system has four distinct states characterized by different Chern numbers and also distinct structures of zero-field Majorana cones: (i) $\mathcal{C} = +1$ and $\{x_{\rm K}, x_+, x_-\}$ ($\zeta < -1$; blue), (ii) $\mathcal{C} = +1$ and $\{x_{\rm K}\}$ ($-1 < \zeta < 1/8$; white), (iii) $\mathcal{C} = -2$ and $\{x_{\rm K}, x_+\}$ ($1/8 < \zeta < 1/3$; red), and (iv) $\mathcal{C} = -2$ and $\{x_{\rm K}, x_+\}$ ($1/3 < \zeta$; red). The energy dispersion $\epsilon(\mathbf{k})$ is illustrated for the four states [(a),(c),(e),(g)] and also at their boundary points [(b),(d),(f)]. In each plot, the energy dispersion is drawn on the gray triangular region centered at the K point of the Brillouin zone (shown in the lower left corner of the figure). **(a),(c),(e),(g)** In most cases, applied magnetic fields gap out the zero-field Majorana cones existing at $h = 0$, whose locations are marked on the Brillouin zone by blue ($\chi = +1$) and red ($\chi = -1$) dots. The black arrows denote the movement directions of the zero-field Majorana cones with increasing ζ. **(b),(f)** At $\zeta = -1$ and $\zeta = 1/3$, the zero-field energy dispersions possess quadratic band touching (QBT), which become gapped out by the applied magnetic field. **(d)** At $\zeta = 1/8$, the zero-field Majorana cones appearing at three M points remain gapless even under the magnetic field. This critical state connects continuously the two neighboring gapped phases with the different Chern numbers, $\mathcal{C} = +1$ and $\mathcal{C} = -2$, via gap closing at the M points.

pair of quadratic band touchings each with a -2π Berry phase, maintaining the $\mathcal{C} = -2$ proximate KSL phase. The other case occurs at $\zeta = -1$ where a x_+ and x_- pair merge at the midpoint of the ΓK (or ΓK′) segment for $h = 0$, but the opposite chiralities for x_+ and x_- AMCs indicate that the $\mathcal{C} = +1$ KSL is maintained. See Fig. 9 for the evolution of the energy dispersion.

- The second example is the case where the electric field and the hydrostatic pressure have equal effects, *i.e.* $D_1 = \Gamma'$ or $\eta = 0$; while this is a case where the definition of $x_\pm$ [Eq. (46)] is invalid, Eqs. (D2), (D3), and (50) still remains valid to the AMCs. Fig. 10 visualizes the topological quantum phase transitions occurring in this case. Details of the change of band topology over four distinct states are discussed below.

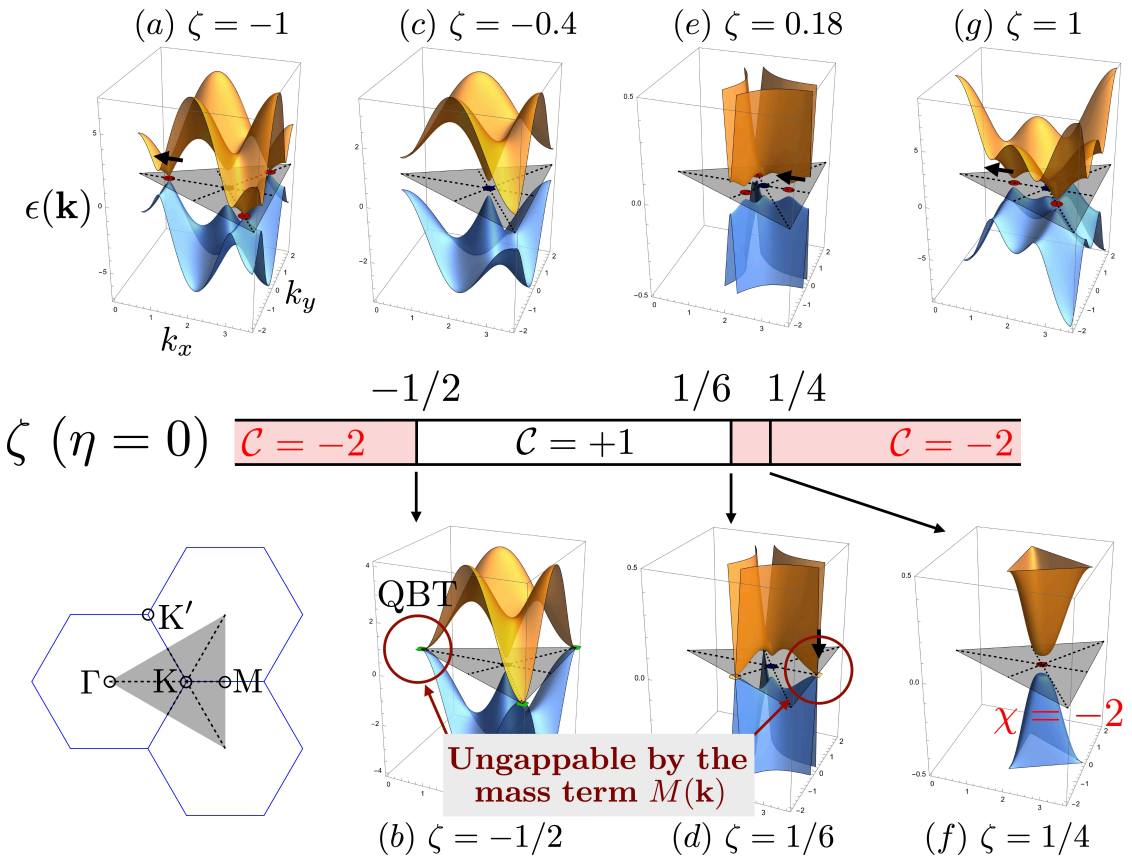


FIG. 10: Topological quantum phase transitions on the $\eta = 0$ line of Fig. 7 in presence of a magnetic field ($h \neq 0$). In the parameter space of $\zeta(\eta = 0)$, the system has four distinct states characterized by different Chern numbers and also distinct structures of zero-field Majorana cones: (i) $\mathcal{C} = -2$ and $\{x_{\rm K}, x\}$ ($\zeta < -1/2$; red), (ii) $\mathcal{C} = +1$ and $\{x_{\rm K}\}$ ($-1/2 < \zeta < 1/6$; white), (iii) $\mathcal{C} = -2$ and $\{x_{\rm K}, x\}$ ($1/6 < \zeta < 1/4$; red), and (iv) $\mathcal{C} = -2$ and $\{x_{\rm K}, x\}$ ($1/4 < \zeta$; red). The energy dispersion $\epsilon(\mathbf{k})$ is illustrated for the four states [(a),(c),(e),(g)] and also at their boundary points [(b),(d),(f)]. In each plot, the energy dispersion is drawn on the gray triangular region centered at the K point of the Brillouin zone (shown in the lower left corner of the figure). **(a),(c),(e),(g)** In most cases, applied magnetic fields gap out the zero-field Majorana cones existing at $h = 0$, whose locations are marked on the Brillouin zone by blue ($\chi = +1$) and red ($\chi = -1$) dots. The black arrows denote the movement directions of the zero-field Majorana cones with increasing ζ. **(b)** At $\zeta = -1/2$, the zero-field energy dispersion possesses quadratic band touching (QBT) at the Γ point, which remain gapless even under the magnetic field. This critical state connects continuously the two neighboring gapped phases with the different Chern numbers, $\mathcal{C} = -2$ and $\mathcal{C} = +1$, via gap closing at the Γ point. **(d)** At $\zeta = 1/6$, the zero-field Majorana cones appearing at three M points remain gapless even under the magnetic field. This critical state connects continuously the two neighboring gapped phases with the different Chern numbers, $\mathcal{C} = +1$ and $\mathcal{C} = -2$, via gap closing at the M points. **(f)** At $\zeta = 1/4$, the zero-field energy dispersion possesses QBT at the K point, which become gapped out by the magnetic field.

$D_1 = \Gamma'$ limit ($\eta = 0$)			
ζ	AMCs	χ	$\mathcal{C}$
$\zeta < -\frac{1}{2}$	$x \in [\Gamma, \mathrm{K}]$	-1	-2
$-\frac{1}{2} < \zeta < \frac{1}{6}$	None		$+1$
$\frac{1}{6} < \zeta < \frac{1}{4}$	$x \in [\mathrm{M}, \mathrm{K}]$	-1	-2
$\zeta > \frac{1}{4}$	$x \in [\Gamma, \mathrm{K}]$	-1	-2

At $\zeta = \frac{1}{6}$, the continuous $\Delta\mathcal{C} = 3$ topological phase transition is again signified by the appearance of an MC at each of the three M points. On the other hand, at $\zeta = -\frac{1}{2}$, the continuous $\Delta\mathcal{C} = 3$ transition signature is the appearance of a Majorana QBT at the Γ point, the details of which is given in Appendix E. In this limit, the merging for $h = 0$ of a AMC trio with the same chirality with K (or K′) occurs at $\zeta = \frac{1}{4}$; it again leads to a quadratic band touching with -2π Berry phase which is gapped out for $h \neq 0$ and maintains the $\mathcal{C} = -2$ proximate KSL. See

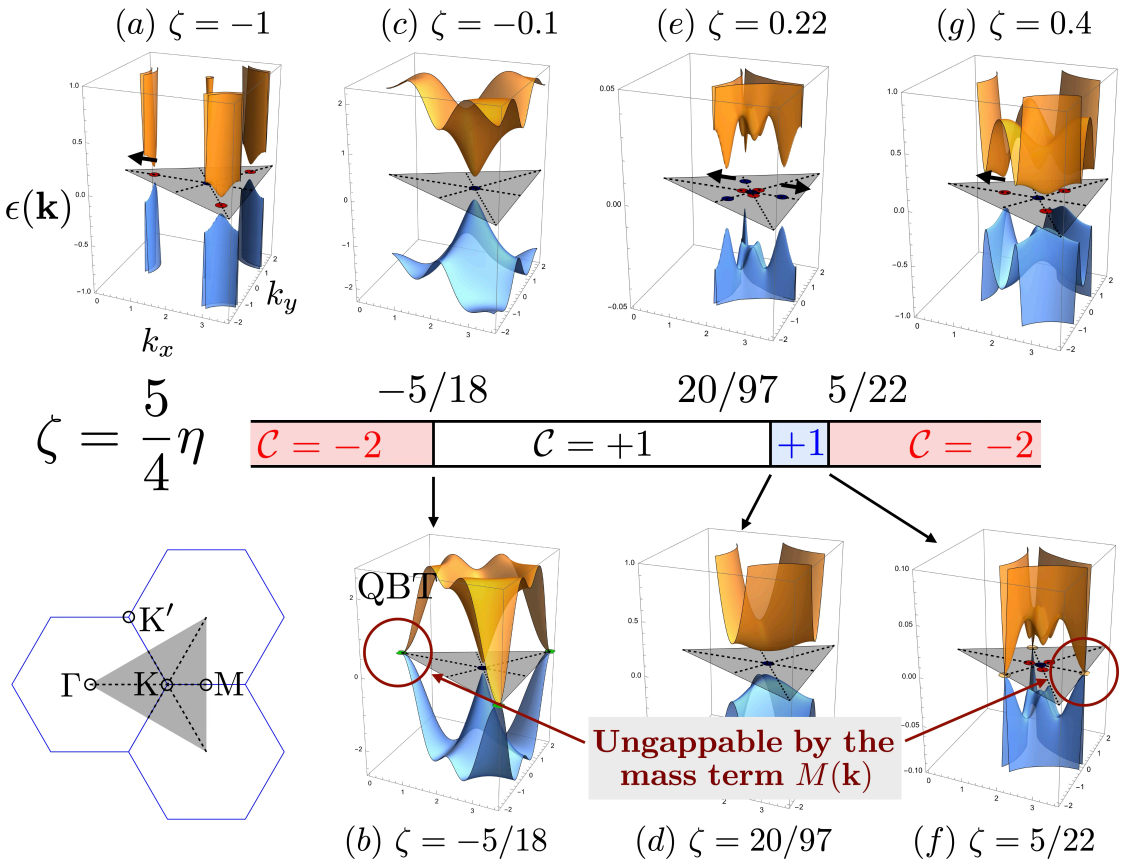


FIG. 11: Topological quantum phase transitions on the $\zeta = 5\eta/4$ line of Fig. 7 in presence of a magnetic field ($h \neq 0$). In the parameter space of $\zeta(= 5\eta/4)$, the system has four distinct states characterized by different Chern numbers and also distinct structures of zero-field Majorana cones: (i) $\mathcal{C} = -2$ and $\{x_{\rm K}, x_-\}$ ($\zeta < -5/18$; red), (ii) $\mathcal{C} = +1$ and $\{x_{\rm K}\}$ ($-5/18 < \zeta < 16/97$; white), (iii) $\mathcal{C} = +1$ and $\{x_{\rm K}, x_+, x_-\}$ ($16/97 < \zeta < 5/22$; blue), and (iv) $\mathcal{C} = -2$ and $\{x_{\rm K}, x_+\}$ ($5/22 < \zeta$; red). The energy dispersion $\epsilon(\mathbf{k})$ is illustrated for the four states [(a),(c),(e),(g)] and also at their boundary points [(b),(d),(f)]. In each plot, the energy dispersion is drawn on the gray triangular region centered at the K point of the Brillouin zone (shown in the lower left corner of the figure). **(a),(c),(e),(g)** In most cases, applied magnetic fields gap out the zero-field Majorana cones existing at $h = 0$, whose locations are marked on the Brillouin zone by blue ($\chi = +1$) and red ($\chi = -1$) dots. The black arrows denote the movement directions of the zero-field Majorana cones with increasing ζ. **(b)** At $\zeta = -1/2$, the zero-field energy dispersion possesses quadratic band touching (QBT) at the Γ point, which remain gapless even under the magnetic field. This critical state connects continuously the two neighboring gapped phases with the different Chern numbers, $\mathcal{C} = -2$ and $\mathcal{C} = +1$, via gap closing at the Γ point. **(d)** At $\zeta = 20/97$, the zero-field energy dispersion possesses a single MC at the K point, which become gapped out by the magnetic field. **(f)** At $\zeta = 5/22$, the zero-field Majorana cones located at three M points remain gapless even under the magnetic field. This critical state connects continuously the two neighboring gapped phases with the different Chern numbers, $\mathcal{C} = +1$ and $\mathcal{C} = -2$, via gap closing at the M points.

Fig. 10 for the evolution of the energy dispersion.

- Lastly, we consider the case of an infinitesimally small hydrostatic pressure ($|\Gamma'| \ll |K|$), *i.e.* $\eta = (1-\delta)\zeta$ ($0 < \delta \ll 1$). Fig. 11 visualizes the topological quantum phase transition occurring in this case. Details of the change of band topology over four distinct states are discussed below.

$\Gamma' \ll \lvert D_1\rvert$ limit [$\eta = (1-\delta)\zeta$]			
ζ	AMCs	χ	$\mathcal{C}$
$\zeta < -\frac{1}{4} - \frac{\delta}{8}$	x_+ doesn't exist		-2
	$x_- \in [\Gamma, \mathrm{K}]$	-1	
$-\frac{1}{4} - \frac{\delta}{8} < \zeta < \frac{1}{5} + \frac{\delta}{25}$	None		$+1$
$\frac{1}{5} + \frac{\delta}{25} < \zeta < \frac{1}{4} - \frac{\delta}{8}$	$x_+ \in [\Gamma, \mathrm{K}]$	-1	$+1$
	$x_- \in [\mathrm{M}, \mathrm{K}]$	$+1$	
$\zeta > \frac{1}{4} - \frac{\delta}{8}$	$x_+ \in [\Gamma, \mathrm{K}]$	-1	-2
	x_- doesn't exist		

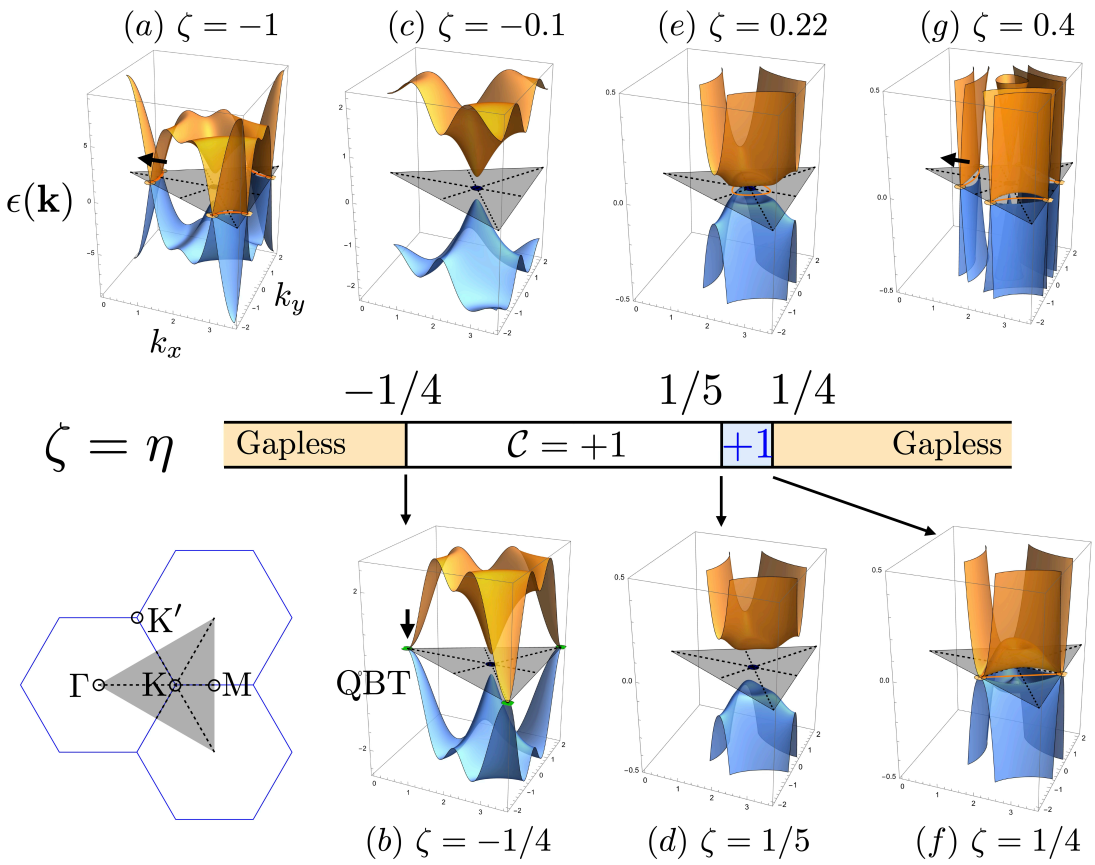


FIG. 12: Topological quantum phase transitions on the $\zeta = \eta$ line of Fig. 7 in presence of a magnetic field ($h \neq 0$). In the parameter space of $\zeta(=\eta)$, the system has four distinct states: (i) gapless ($\zeta < -1/4$; yellow), (ii) gapped with $\mathcal{C} = +1$ ($-1/4 < \zeta < 1/5$; white), (iii) gapped with $\mathcal{C} = +1$ ($1/5 < \zeta < 1/4$; blue), and (iv) gapless ($1/4 < \zeta$; yellow). At zero field, except in the region of $-1/4 < \zeta < 1/5$, Majorana fermi line nodes arise in the energy spectrum as described by Eq. (51); denoted by orange lines on the Brillouin zone. Under the magnetic field, the line nodes are mostly gapped out. Only the intersections of the line nodes with the ΓM lines remain gapless, leading to the gapless states in the yellow regions of the parameter space. In the other regions, the line nodes are all gapped out, resulting in the gapped states with the Chern number $\mathcal{C} = +1$. The energy dispersion $\epsilon(\mathbf{k})$ is illustrated for the four states [(a),(c),(e),(g)] and also at their boundary points [(b),(d),(f)]. In each plot, the energy dispersion is drawn on the gray triangular region centered at the K point of the Brillouin zone (shown in the lower left corner of the figure).

Once again, the continuous $\Delta\mathcal{C} = 3$ topological phase transition is signified by the appearance of an MC each of the three M points for $\zeta = \frac{1}{4} - \frac{\delta}{8}$ and the Majorana QBT at the Γ point for $\zeta = -\frac{1}{4} - \frac{\delta}{8}$. However, merging of two AMC trios with the opposite chirality near K (or K′) at $\zeta = \frac{1}{5} + \frac{\delta}{25}$ for $h = 0$ leads to a band touching with 0 Berry phase which is trivially gapped out for $h \neq 0$ and maintains the $\mathcal{C} = +1$ KSL. See Fig. 11 for the evolution of the energy dispersion for an example where $\delta = \frac{1}{5}$.

When the hydrostatic pressure is entirely absent, *i.e.* $\Gamma' = 0$, the Majorana line node of Eq. (51) is gapped out by the purely Zeeman mass term $\delta M(\mathbf{k}) = \frac{72h^3}{\Delta^2}\sum_{m=1}^{3}\sin\left[\mathbf{k}\cdot\mathbf{d}_m^{(2)}\right]$ which adds to $M(\mathbf{k})$ at the level of the third-order perturbation [1], except for the point nodes appearing at a few critical ζ value, as shown in Fig. 12; note also that for $\Gamma' \leq 0$ there will be no gap closing in $0 < |\zeta/\eta - 1| \ll 1$, as $\frac{\delta M(\mathbf{k})}{M(\mathbf{k})} = -\frac{\Gamma'\Delta}{18\sqrt{3}h^2} > 0$ would always hold in that case. We note that a 3D analogue of this case has been discussed in the hyperhoneycomb lattice [50]. Point nodes in presence of $\delta M(\mathbf{k})$ arise if the Eq. (51) Majorana line node intersects with the ΓM lines where $\delta M(\mathbf{k})$ vanishes. As Eq. (51) gives us no intersection at all for $|\zeta| < \frac{1}{4}$, the Chern number $\mathcal{C} = +1$ of the KSL phase is maintained for this range of ζ, as illustrated in Fig. 12. By contrast, for $|\zeta| > \frac{1}{4}$, the Majorana line node of Eq. (51) forms a closed loop around Γ, thereby giving us a sextet of intersection points

with the ΓM line, as illustrated in Fig. 12. This can be attributed to, as implied by Eq. (50), the existence of a $\mathcal{C} = +4$ phase on the other side of $\zeta = \eta$ for $|\zeta| > \frac{1}{4}$ due to the change of the x_+ chirality, had $|\zeta| < |\eta|$ been physical. Fig. 12 (f) shows that at $\eta = +\frac{1}{4}$, where the Majorana line node goes from encircling K to encircling Γ, the MCs merge in pairs to leave an MC at each of three M points. Meanwhile at $\eta = -\frac{1}{4}$, Fig. 12 (b) shows that, as the Majorana line node shrinks and converges into the Γ point, all six MCs merge into a quadratic Majorana band touching at Γ.

We note that within the zero flux sector there is a limitation on the possible Chern numbers for the proximate KSL. From our perturbation theory in the zero flux sector, either the AMCs exist in a trio for each valley with the chirality opposite of the original MC at K or K′ or the total chiralities of AMCs cancel out, as shown in Fig. 7. This implies that the continuous quantum phase transition from the KSL to the proximate KSL in our model would always involve the change of the Chern number from ± 1 to ∓ 2 with the Chern number sign always reversed. This is in contrast with the proximate KSL phases found from the variational Monte Carlo calculations [24, 25] where discontinuous quantum phase transitions involving the entry of the $\mathbb{Z}_2$ flux entry result in the proximate KSL phases with the Chern number of ± 4, ± 5, and ∓ 8. In other words, our proximate KSL is always Abelian and therefore the continuous topological phase transition we have obtained is between a non-Abelian phase and an Abelian phase.

IV. CONCLUSIONS AND DISCUSSION

We have presented a study of the perturbation effect of the DM and the Γ' interaction on the zero-flux sector, the main feature of which is a continuous topological phase transition from the non-Abelian $\mathcal{C} = \pm 1$ KSL to the Abelian $\mathcal{C} = \mp 2$ proximate KSL. The key step here is that on the zero flux sector, both the DM and the Γ' interaction contribute nothing at the first order but the third and the fourth neighbor Majorana hopping at the second order. When the magnitude of these distant Majorana hopping amplitude grows sufficiently large, the AMCs emerge, which translates into the topological phase transition when $h \neq 0$.

Our perturbative approach enabled us to scan possibilities of topological phase transitions over all ranges of parameters satisfying $|D_1|, |\Gamma'| \ll |K|$. Given the nature of perturbative approach, our chief aim is to complement various numerical analysis, *e.g.* the exact numerical calculation results on the effect of similar 4-spin interactions on the KSL [43, 51] where the two 4-spin interaction parameters were fixed to have the opposite signs (corresponding to $|D_1| > |\Gamma'|$ in our model), by examining parameter regions that were left unexplored. Our hope is that this work in turn will serve as a guide for future numerical analysis on the effects of the DM and the Γ' interactions that will verify the existence of the continuous topological quantum phase transitions we have discussed.

Tuning electric field and hydrostatic pressure will give us physical access over the (η, ζ) space of Fig. 7, albeit with a few limitations. From the definition of Eq. (42), we can see that tuning the perpendicular electric field, through D_1, will allow us to move in the (η, ζ) space parallel to $\zeta = \eta$, while tuning the hydrostatic pressure, through Γ', will allow us to move parallel to $\zeta = -\eta$ (see Appendix A and B for details on the effect of electric field and hydrostatic pressure on D_1 and Γ', respectively, through the modifying the nearest-neighbor electron hopping). However, this does not provide us with any method to change the sign of ζ. From Eq. (42), we can expect $\zeta > 0$ from the antiferromagnetic Kitaev interaction $\zeta < 0$ from the ferromagnetic Kitaev interaction. Fig. 7 suggests that the best bet for accessing our continuous topological phase transition would be to either start from the antiferromagnetic Kitaev interaction or stay near $\zeta = \eta$, *i.e.* $|D_1| \gg \Gamma'$.

Transition between the $\mathcal{C} = \pm 1$ KSL and the $\mathcal{C} = \mp 2$ proximate KSL should be manifest in thermal transport measurement. There has been extensive theoretical discussion, with Refs. [1, 52] only being most cited examples, on the ratio of thermal Hall conductivity to temperature at low temperatures being proportional to $\mathcal{C}$ $[\kappa_{xy}/T = \mathcal{C}(\pi/12)(k_B^2/\hbar)]$, which in more recent years, has also been investigated experimentally [12, 13, 15]. In the context of our results, this implies that the $\mathcal{C} = \pm 1$ to $\mathcal{C} = \mp 2$ transition involves thermal Hall conductivity both reversing its sign and doubling its magnitude.

Additionally, we would like to point out that our *continuous* topological phase transition through uniform parameter tuning suggest the possibility of adiabatic deformation and transport of topological domains through tuning non-uniform parameter. For example, moving a finite domain with stronger electric field can lead to *adiabatic* transport of an Abelian $\mathcal{C} = \mp 2$ domain against the non-Abelian $\mathcal{C} = \pm 1$ background with three, *odd*, branches of chiral Majorana modes along its boundary. It has been proposed that such adiabatic deformation of Abelian domains in KSL can be used for fusing a pair of Majorana zero modes [44] and adiabatically transporting a Majorana zero mode [45]. Hence, our results suggest that topologically protected quantum gates can be realized in the KSL by locally applying electric field or hydrostatic pressure.

ACKNOWLEDGMENTS

We thank Jason Alicea, Minchul Lee, Yuji Matsuda and Pureum Noh for sharing their insights. S.J.K. was supported by the Graduate School of Engineering, The University of Tokyo Doctoral Student Special Incentives Program (SEUT-RA). S.B.C. was supported by the National Research Foundation of Korea (NRF)

grants funded by the Korea government (MSIT) (NRF-2023R1A2C1006144 and NRF-2020R1A2C1007554).

Appendix A: HOPPING MATRIX AND SPIN INTERACTION PARAMETERS

In Kitaev materials, the hopping of d-orbital electrons create effective spin interactions. [16, 23] When an electric field is applied to a system, the inversion symmetry of the system is broken by the external field. The breaking of inversion symmetry implies a distortion of the orbitals pushed by the electric field, or the appearance of electric polarization. [53] Due to this effect on the atomic orbitals, an additional hopping of electrons, which is forbidden by symmetry in the absence of electric fields, emerges as a result of inversion symmetry breaking. For simplicity, we consider the bonding of only two transition atoms, i.e., Z-bonding. The hopping matrix T_Z of the Z-bonding system, written in the t_{2g} basis without external electric fields, is given by [16]

$$T_Z = \begin{pmatrix} t_1 & t_2 & 0 \\ t_2 & t_1 & 0 \\ 0 & 0 & t_3 \end{pmatrix} \tag{A1}$$

If an electric field is applied, the inversion symmetry-breaking hopping will be introduced. To consider a simple model, we assume that the electric field is applied perpendicular to the sample. To describe the effect of the electric field, we need to adopt two types of coordinate. The first is the xyz-coordinate which is consistent with the direction of the d-orbitals. The second is the uvw-coordinate, defined as [28, 29]

$$\hat{u} = \frac{\hat{x} - \hat{y}}{\sqrt{2}},\ \hat{v} = \frac{\hat{x} + \hat{y}}{\sqrt{2}},\ \hat{w} = \hat{z} \tag{A2}$$

The electric field perpendicular to a sample is given by

$$\vec{E} = \frac{E}{\sqrt{3}}\hat{x} + \frac{E}{\sqrt{3}}\hat{y} + \frac{E}{\sqrt{3}}\hat{z} \tag{A3}$$

In the xyz-coordinate system, the hopping matrix with inversion symmetry breaking is given by

$$T_Z = \begin{pmatrix} t_1 & t_2 - t_w & t_4 - \sqrt{2}t' \\ t_2 + t_w & t_1 & t_4 + \sqrt{2}t' \\ t_4 + \sqrt{2}t' & t_4 - \sqrt{2}t' & t_3 \end{pmatrix} \tag{A4}$$

where $t_u = -t_v = t'$ and t_w are the hoppings induced by inversion symmetry breaking, and t_4 is the hopping caused by the trigonal distortion.

Following the second order perturbation analysis, we can calculate the interaction coefficients of the spin Hamiltonian in terms of the hopping parameter defined in Eq. (A4). In particular, the DM interaction coefficients are given by [16, 23]

$$D_z^x = D_z^y = \frac{16\sqrt{2}}{9}\left[\mathbb{A}(2t_1 + t_3) + \mathbb{B}(t_1 + \frac{t_2}{3} - t_3)\right]t' - \frac{16\mathbb{B}}{3}t_4 t_w \tag{A5}$$

$$D_z^z = \frac{16}{9}\left[-\mathbb{A}(2t_1 + t_3) + 2\mathbb{B}(t_1 - t_3)\right]t_w \tag{A6}$$

where $\mathbb{A}$ and $\mathbb{B}$ are coefficients that include Hund's coupling J_H, Coulomb coupling U, and spin-orbit coupling λ, and the subscript z denotes coefficients at z-linked system.

$$\begin{aligned} \mathbb{A} &= -\frac{1}{3}\left[\frac{J_H + 3(U + 3\lambda)}{6J_H^2 - U(U + 3\lambda) + J_H(U + 4\lambda)}\right] \\ \mathbb{B} &= \frac{4}{3}\left[\frac{3J_H - U - 3\lambda}{6J_H - 2U - 3\lambda}\eta\right] \\ \eta &= \frac{J_H}{6J_H^2 - J_H(8U + 17\lambda) + (2U + 3\lambda)(U + 3\lambda)} \end{aligned}$$

Since Eq. (A5) and Eq. (A6) implies that the DM interaction is described by two parameters, we define $D_1 = D_z^x = D_z^y$ and $D_2 = D_z^z$. For the system has C_3-symmetry, interaction coefficients are not depend on the bonding direction, so we can define $K_\alpha = K$, $\Gamma_\alpha^{\beta\gamma} = \Gamma$, $\Gamma_\alpha^{\alpha\beta} = \Gamma_\alpha^{\gamma\alpha} = \Gamma'$ and these coefficients also can be obtained by the second order perturbation theory.

$$\begin{aligned} K &= \frac{32\mathbb{A}}{9}(t_w^2 - 2t'^2) + \frac{8\mathbb{B}}{9}\left[3(t_1 - t_3)^2 - 9t_2^2 + 9t_4^2 + 2t'^2 - t_w^2\right] \\ \Gamma &= \frac{64\mathbb{A}}{9}t'^2 + \frac{8\mathbb{B}}{9}\left[6(t_1 - t_3)t_2 + 9t_4^2 - 2t'^2\right] \\ \Gamma' &= -\frac{32\sqrt{2}\mathbb{A}}{9}t' t_w - \frac{8\mathbb{B}}{9}\left[3(t_1 - t_3)t_4 - 9t_2 t_4 - \sqrt{2}t' t_w\right] \\ J &= \frac{4\mathbb{A}}{9}\left[(2t_1^2 + t_3)^2 - 4t_w^2\right] - \frac{8\mathbb{B}}{9}\left[2(t_1 - t_3)^2 + 9t_4^2 - 6t'^2 - 2t_w^2\right] \end{aligned}$$

Appendix B: INVERSION SYMMETRY BREAKING HOPPING PARAMETERS

In the Z-bonding system, we can define two types of coordinates, the uvw-coordinate and the xyz-coordinate. The xyz-coordinate is consistent with the direction of the d-orbitals. At first, we will consider the hopping matrix in the uvw-coordinate without the electric field, but with trigonal distortion. [28]

$$T_Z = \begin{pmatrix} t_{11} & 0 & 0 \\ 0 & t_{22} & \tilde{t} \\ 0 & \tilde{t} & t_{33} \end{pmatrix}_{uvw} \tag{B1}$$

The subscript uvw indicates that the matrix is expressed in the uvw-coordinate system. In the xyz-coordinate, the hopping matrix is converted into the well known form as [39]

$$T_Z = \begin{pmatrix} \frac{t_{11}+t_{22}}{2} & \frac{-t_{11}+t_{22}}{2} & \frac{\tilde{t}}{\sqrt{2}} \\ \frac{-t_{11}+t_{22}}{2} & \frac{t_{11}+t_{22}}{2} & \frac{\tilde{t}}{\sqrt{2}} \\ \frac{\tilde{t}}{\sqrt{2}} & \frac{\tilde{t}}{\sqrt{2}} & t_{33} \end{pmatrix}_{xyz} = \begin{pmatrix} t_1 & t_2 & t_4 \\ t_2 & t_1 & t_4 \\ t_4 & t_4 & t_3 \end{pmatrix}_{xyz} \tag{B2}$$

where the substitutions $t_1 = \frac{t_{11}+t_{22}}{2}$, $t_2 = \frac{-t_{11}+t_{22}}{2}$, $t_3 = t_{33}$ and $t_4 = \frac{\tilde{t}}{\sqrt{2}}$ are used.

Next, we consider the hopping induced by inversion symmetry breaking. They will given by [28]

$$T_u = \begin{pmatrix} 0 & 0 & -t_u \\ 0 & 0 & -t_u \\ t_u & t_u & 0 \end{pmatrix}_{uvw} \tag{B3}$$

$$T_v = \begin{pmatrix} 0 & 0 & t_v \\ 0 & 0 & -t_v \\ -t_v & t_v & 0 \end{pmatrix}_{uvw} \tag{B4}$$

$$T_w = \begin{pmatrix} 0 & -t_w & 0 \\ t_w & 0 & 0 \\ 0 & 0 & 0 \end{pmatrix}_{uvw} \tag{B5}$$

Add these equations to Eq. (B2) and convert them into the XYZ-coordinate.

$$\begin{aligned} T_Z &= \begin{pmatrix} t_{11} & -t_w & -t_u+t_v \\ t_w & t_{22} & \tilde{t}-t_u-t_v \\ t_u-t_v & \tilde{t}+t_u+t_v & t_{33} \end{pmatrix}_{uvw} \\ &= \begin{pmatrix} t_1 & t_2-t_w & t_4-\sqrt{2}t_u \\ t_2+t_w & t_1 & t_4-\sqrt{2}t_v \\ t_4+\sqrt{2}t_u & t_4+\sqrt{2}t_w & t_3 \end{pmatrix}_{xyz} \end{aligned} \tag{B6}$$

In addition to considering mirror symmetry between the transition atoms, i.e., $t_u = -t_v = t'$, the final form of the hopping matrix is given by

$$T_Z = \begin{pmatrix} t_1 & t_2-t_w & t_4-\sqrt{2}t' \\ t_2+t_w & t_1 & t_4+\sqrt{2}t' \\ t_4+\sqrt{2}t' & t_4-\sqrt{2}t' & t_3 \end{pmatrix}_{xyz} \tag{B7}$$

Appendix C: GENERIC PERTURBATION OF SPIN HAMILTONIAN

In this section, we will show the perturbation approach in section III-(B-E) without C_3-rotational symmetries. The model Hamiltonian without C_3 symmetry is given by the combination of the following

$$\begin{aligned} H_K^\alpha &= \sum_{\langle i,j\rangle_\alpha} K_\alpha \sigma_i^\alpha \sigma_j^\alpha \\ H_\Gamma^\alpha &= \sum_{\langle i,j\rangle_\alpha} \sum_{\beta\neq\alpha} \sum_{\gamma\neq\alpha,\beta} \Gamma_\alpha^{\beta\gamma} (\sigma_i^\beta \sigma_j^\gamma + \sigma_i^\gamma \sigma_j^\beta)/2 \\ H_{\Gamma'}^\alpha &= \sum_{\langle i,j\rangle_\alpha} \sum_{\beta\neq\alpha} \Gamma_\alpha^{\alpha\beta} (\sigma_i^\alpha \sigma_j^\beta + \sigma_i^\beta \sigma_j^\alpha) \\ H_D^\alpha &= \sum_{\langle i,j\rangle_\alpha} \sum_{\beta,\gamma} \varepsilon_{\alpha\beta\gamma} \left[D_\alpha^\alpha \sigma_i^\beta \sigma_j^\gamma + D_\alpha^\beta (\sigma_i^\gamma \sigma_j^\alpha - \sigma_i^\alpha \sigma_j^\gamma) \right] \\ H_Z &= -\sum_i (h_x \sigma_i^x + h_y \sigma_i^y + h_z \sigma_i^z), \end{aligned}$$

of which the first gives us the zeroth order term, *i.e.* $H_0 = \sum_\alpha H_K^\alpha$.

The nearest-neighbor Majorana hopping contribution from the second-order perturbation in the zero-flux sector by the product of a pair of Zeeman terms is given by

$$H_{ZZ} = \sum_{\langle A,B\rangle_\alpha} P_0 \frac{h_\alpha^2}{\Delta} \sigma_A^\alpha \sigma_B^\alpha P_0 = -\frac{2i}{\Delta} \sum_{\langle A,B\rangle_\alpha} h_\alpha^2 c_A c_B \tag{C1}$$

The nearest-neighbor Majorana hopping contribution from the second-order perturbation in the zero-flux sector by the product of a pair of spin interactions belonging to the D_2-type as defined by the Tab. II is given by

$$\begin{aligned} H_{D_2D_2}^\alpha &= \sum_{\langle A,B\rangle_\alpha} \sum_{\beta\neq\alpha} \sum_{\gamma\neq\alpha,\beta} P_0 \left[\frac{(\Gamma_\alpha^{\beta\gamma} + D_\alpha^\alpha)(\Gamma_\alpha^{\beta\gamma} - D_\alpha^\alpha)}{\Delta} \left(\sigma_A^\beta \sigma_B^\gamma \sigma_A^\gamma \sigma_B^\beta + \sigma_A^\gamma \sigma_B^\beta \sigma_A^\beta \sigma_B^\gamma \right) \right] P_0 \\ &= \sum_{\langle A,B\rangle_\alpha} \frac{2\left[\left(\Gamma_\alpha^{\beta\gamma}\right)^2 - \left(D_\alpha^\alpha\right)^2 \right]}{\Delta} P_0 \sigma_A^\alpha \sigma_B^\alpha P_0 \\ &= \sum_{\langle A,B\rangle_\alpha} \frac{2i\left[\left(D_\alpha^\alpha\right)^2 - \left(\Gamma_\alpha^{\beta\gamma}\right)^2 \right]}{\Delta} c_A c_B \end{aligned} \tag{C2}$$

The third-neighbor Majorana hopping contribution from the second-order perturbation in the zero-flux sector by

the product of a pair of spin interactions belonging to the D_1/Γ' type as defined by the Tab. II is given by

$$\begin{aligned} H^{(3),\alpha\beta}_{\Gamma'\Gamma'} &= \sum_{\langle ABA'B'\rangle_{\alpha\gamma\beta}} P_0 \left[\frac{2(\Gamma^{\alpha\beta}_{\alpha}+D^{\gamma}_{\alpha})(\Gamma^{\alpha\beta}_{\beta}+D^{\gamma}_{\beta})}{\Delta}\sigma^{\alpha}_{A}\sigma^{\beta}_{B}\sigma^{\alpha}_{A'}\sigma^{\beta}_{B'} + \frac{2(\Gamma^{\alpha\beta}_{\alpha}-D^{\gamma}_{\alpha})(\Gamma^{\alpha\beta}_{\beta}-D^{\gamma}_{\beta})}{\Delta}\sigma^{\beta}_{A}\sigma^{\alpha}_{B}\sigma^{\beta}_{A'}\sigma^{\alpha}_{B'} \right] P_0 \\ &= \sum_{\langle A,B\rangle_{3,\alpha\beta}} \sum_{\gamma\neq\alpha,\beta} \frac{4i(\Gamma^{\alpha\beta}_{\alpha}\Gamma^{\alpha\beta}_{\beta}+D^{\gamma}_{\alpha}D^{\gamma}_{\beta})}{\Delta} c_A c_B \end{aligned} \tag{C3}$$

where $\langle A,B\rangle_{3,\alpha\beta}$ implies that the third-neighbor pairs with the combination of the α-link and β-link at the beginning and the ending or vice versa; note that the figures both Eqs. (26) and (27) would give us $\alpha = x$ and $\beta = y$.

The fourth-neighbor Majorana hopping contribution from the second-order perturbation in the zero-flux sector by the product of a pair of spin interactions belonging to the D_1/Γ' type by the Tab. II is given as

$$\begin{aligned} H^{(4),\alpha}_{\Gamma'\Gamma'} &= \sum_{\langle ABA'B'\rangle_{\alpha\gamma\alpha}} \sum_{\beta\neq\gamma} \frac{2\left\{\left(\Gamma^{\alpha\beta}_{\alpha}\right)^2-\left(D^{\gamma}_{\alpha}\right)^2)\right\}}{\Delta} P_0\sigma^{\alpha}_{A}\sigma^{\beta}_{B}\sigma^{\beta}_{A'}\sigma^{\alpha}_{B'}P_0 + \sum_{\langle ABA'B'\rangle_{\alpha\beta\alpha}} \sum_{\gamma\neq\beta} \frac{2\left\{(\Gamma^{\gamma\alpha}_{\alpha})^2-\left(D^{\beta}_{\alpha}\right)^2)\right\}}{\Delta} P_0\sigma^{\gamma}_{A}\sigma^{\alpha}_{B}\sigma^{\alpha}_{A'}\sigma^{\gamma}_{B'}P_0 \\ &= \sum_{\langle A,B\rangle_{4,\alpha\beta}} \frac{2i\left[\left(D^{\gamma}_{\alpha}\right)^2-\left(\Gamma^{\alpha\beta}_{\alpha}\right)^2\right]}{\Delta} c_A c_B + \sum_{\langle A,B\rangle_{4,\alpha\gamma}} \frac{2i\left[\left(D^{\beta}_{\alpha}\right)^2-\left(\Gamma^{\gamma\alpha}_{\alpha}\right)^2\right]}{\Delta} c_A c_B \end{aligned} \tag{C4}$$

where $\langle A,B\rangle_{4,\alpha\beta}$ represents a fourth-neighbor pair linked by the initial and the final α-links with a β-link coming in between.

The second-neighbor Majorana hopping contribution from the second-order perturbation in the zero-flux sector by the prduct of one Zeeman-type and one Γ-type spin interactions is given by

$$\begin{aligned} H^{(2),\alpha}_{Z\Gamma'} =& P_0 \left[\sum_{\langle ABA'\rangle_{\alpha\gamma}} \sum_{\beta\neq\alpha,\gamma} \frac{2(\Gamma^{\alpha\beta}_{\alpha}+D^{\gamma}_{\alpha})h^{\gamma}}{\Delta}\sigma^{\alpha}_{A}\sigma^{\beta}_{B}\sigma^{\gamma}_{A'} + \sum_{\langle BAB'\rangle_{\beta\alpha}} \sum_{\gamma\neq\alpha,\beta} \frac{2(\Gamma^{\gamma\alpha}_{\alpha}+D^{\beta}_{\alpha})h^{\beta}}{\Delta}\sigma^{\gamma}_{A}\sigma^{\beta}_{B}\sigma^{\alpha}_{B'} \right. \\ &\left. + \sum_{\langle BAB'\rangle_{\alpha\gamma}} \sum_{\beta\neq\alpha,\gamma} \frac{2(\Gamma^{\alpha\beta}_{\alpha}-D^{\alpha}_{\gamma})h^{\gamma}}{\Delta}\sigma^{\beta}_{A}\sigma^{\alpha}_{B}\sigma^{\gamma}_{B'} + \sum_{\langle ABA'\rangle_{\beta\alpha}} \sum_{\gamma\neq\alpha,\beta} \frac{2(\Gamma^{\gamma\alpha}_{\alpha}-D^{\alpha}_{\beta})h^{\beta}}{\Delta}\sigma^{\beta}_{A}\sigma^{\gamma}_{B}\sigma^{\alpha}_{A'} \right] P_0 \end{aligned} \tag{C5}$$

from which we obtain

$$\begin{aligned} H^{(2)}_{Z\Gamma'} =& \left[\sum_{\langle A,A'\rangle_{2,zx}} \frac{2i\left\{(\Gamma^{xy}_{x}+D^{z}_{x})h^{z}+(\Gamma^{yz}_{z}-D^{x}_{z})h^{x}\right\}}{\Delta} + \sum_{\langle A,A'\rangle_{2,yz}} \frac{2i\left\{(\Gamma^{zx}_{z}+D^{y}_{z})h^{y}+(\Gamma^{xy}_{y}-D^{z}_{y})h^{z}\right\}}{\Delta} \right. \\ &\left. + \sum_{\langle A,A'\rangle_{2,xy}} \frac{2i\left\{(\Gamma^{yz}_{y}+D^{x}_{y})h^{x}+(\Gamma^{zx}_{x}-D^{y}_{x})h^{y}\right\}}{\Delta} \right] c_A c_{A'} \\ &+ \left[\sum_{\langle B,B'\rangle_{2,zx}} \frac{2i\left\{(\Gamma^{xy}_{y}+D^{z}_{y})h^{z}+(\Gamma^{yz}_{z}-D^{x}_{z})h^{x}\right\}}{\Delta} + \sum_{\langle B,B'\rangle_{2,yz}} \frac{2i\left\{(\Gamma^{zx}_{z}+D^{y}_{z})h^{y}+(\Gamma^{xy}_{y}-D^{z}_{y})h^{z}\right\}}{\Delta} \right. \\ &\left. + \sum_{\langle B,B'\rangle_{2,xy}} \frac{2i\left\{(\Gamma^{yz}_{z}+D^{x}_{z})h^{x}+(\Gamma^{zx}_{x}-D^{y}_{x})h^{y}\right\}}{\Delta} \right] c_B c_{B'} \end{aligned} \tag{C6}$$

where $\langle A,A'\rangle_{2,\alpha\beta}$ and $\langle B,B'\rangle_{2,\alpha\beta}$ imply that the second-neighbor pairs with the combination of the α-link and the β-link term at the beginning and the ending or vice versa; note that the figures both Eqs. (23) and (24) would give us $\alpha = x$, $\beta = z$ and $\alpha = z$, $\beta = x$.

Appendix D: EXPLICIT AMC CONDITION AT $h = 0$

The reality condition, $x_{\pm} \in \mathbb{R}$, leads to the constraint,

$$x_{\pm} \in \mathbb{R}: \qquad \left(\left|\eta-\frac{1}{2}\right| \leq \frac{1}{2} \text{ and } |\zeta+\eta| \geq \sqrt{\eta-\eta^2}\right) \text{ or } \left(\left|\eta-\frac{1}{2}\right| \geq \frac{1}{2}\right). \tag{D1}$$

From the condition, $|x_\pm| \le 1$, we obtain two more constraints,

$$|x_+| \le 1: \quad \left[\eta \ge 0 \text{ and } \left(-2\zeta \le \zeta \le 2\eta \text{ and } \zeta \ge -\eta - \frac{1}{2}\right)\right] \text{ or } \left(\zeta \ge \frac{1}{6} + \frac{1}{3}\eta\right), \tag{D2}$$

and

$$|x_-| \le 1: \quad \left[\eta \ge 0 \text{ and } \left(-2\zeta \le \zeta \le 2\eta \text{ and } \zeta \le \frac{1}{6} + \frac{1}{3}\eta\right)\right] \text{ or } \left(\zeta \le -\eta - \frac{1}{2}\right). \tag{D3}$$

By combining Eqs. (D1), (D2), (D3), and (50) with $\zeta^2 > \eta^2$ from the definition of ζ and η [47], it is possible to determine the type and the chirality of any AMCs that may exist for given ζ and η. We thereby obtain the full, the explicit condition for the existence of the x_+ AMCs with negative chirality in the K valley to be

$$\begin{aligned}
&\left(\eta \ge \frac{1}{5} \text{ and } \zeta > \eta\right) \text{ or} \\
&\left[\frac{1}{10} \le \eta < \frac{1}{5} \text{ and } \left(\sqrt{\eta - \eta^2} - \eta < \zeta < \frac{1}{4} - \frac{1}{4}\eta \text{ or } \zeta > \frac{1}{4} - \frac{1}{4}\eta\right)\right] \text{ or} \\
&\left[-\frac{1}{8} \le \eta < \frac{1}{10} \text{ and } \left(\frac{1}{6} + \frac{1}{3}\eta < \zeta < \frac{1}{4} - \frac{1}{4}\eta \text{ or } \zeta > \frac{1}{4} - \frac{1}{4}\eta\right)\right] \text{ or} \\
&\left[-\frac{1}{3} \le \eta < -\frac{1}{8} \text{ and } \left(-\eta \le \zeta < \frac{1}{4} - \frac{1}{4}\eta \text{ or } \zeta > \frac{1}{4} - \frac{1}{4}\eta\right)\right] \text{ or} \\
&\left(\eta < -\frac{1}{3} \text{ and } \zeta \ge -\eta\right),
\end{aligned} \tag{D4}$$

that of the existence of the x_+ AMCs with positive chirality in the K valley to be

$$\begin{aligned}
&\left(\eta > 1 \text{ and } -\eta - \frac{1}{2} < \zeta \le -\eta\right) \text{ or} \\
&\left(\frac{1}{2} < \eta \le 1 \text{ and } -\eta - \frac{1}{2} < \zeta < -\sqrt{\eta - \eta^2} - \eta\right),
\end{aligned} \tag{D5}$$

that of the existence of the x_- AMCs with positive chirality in the K valley to be

$$\begin{aligned}
&\left(\frac{1}{5} \le \eta \le \frac{1}{4} \text{ and } \eta < \zeta < \frac{1}{6} + \frac{1}{3}\eta\right) \text{ or} \\
&\left[\frac{1}{7} < \eta < \frac{1}{5} \text{ and } \left(\sqrt{\eta - \eta^2} - \eta < \zeta < \frac{1}{4} - \frac{1}{4}\eta \text{ or } \frac{1}{4} - \frac{1}{4}\eta < \zeta < \frac{1}{6} + \frac{1}{3}\eta\right)\right] \text{ or} \\
&\left(\frac{1}{10} < \eta \le \frac{1}{7} \text{ and } \sqrt{\eta - \eta^2} - \eta < \zeta < \frac{1}{6} + \frac{1}{3}\eta\right).
\end{aligned} \tag{D6}$$

and that of the existence of the x_- AMCs with negative chirality in the K valley to be

$$\begin{aligned}
&(\eta > 1 \text{ and } \zeta \le -\eta) \text{ or} \\
&\left(\frac{1}{2} < \eta \le 1 \text{ and } \zeta < -\sqrt{\eta - \eta^2} - \eta\right) \text{ or} \\
&\left(-\frac{1}{4} < \eta \le \frac{1}{2} \text{ and } \zeta < -\eta - \frac{1}{2}\right) \text{ or} \\
&\left(\eta \le -\frac{1}{4} \text{ and } \zeta < \eta\right).
\end{aligned} \tag{D7}$$

Appendix E: GAP CLOSING AT TOPOLOGICAL QUANTUM PHASE TRANSITIONS

We examine here the energy gap closings occurring at M for $\zeta = \frac{1}{6} + \frac{1}{3}\eta$ and the other occurring at Γ for $\zeta = -\frac{1}{2} - \eta$. This can be most easily done by expanding

$$\mathcal{F}(\mathbf{k}) \cdot \boldsymbol{\sigma} = \begin{pmatrix} M(\mathbf{k}) & f(\mathbf{k}) \\ f^*(\mathbf{k}) & -M(\mathbf{k}) \end{pmatrix} \tag{E1}$$

around M for $\zeta = \frac{1}{6} + \frac{1}{3}\eta$ and around Γ for $\zeta = -\frac{1}{2} - \eta$.

To consider $\mathcal{F}(\mathbf{k})$ around M for $\zeta = \frac{1}{6} + \frac{1}{3}\eta$, we can take $\mathbf{k} = \hat{\mathbf{x}}2\sqrt{3}\pi + \delta\mathbf{q}$ and find up to the first order

$$\begin{aligned} f_1(\mathbf{k}) &= -iK_1 \sum_{m=1}^{3} e^{-i\mathbf{k}\cdot\mathbf{d}_m^{(1)}} \\ &= -iK_1 \sum_{m=1}^{3} e^{-i(\hat{\mathbf{x}}2\sqrt{3}\pi+\delta\mathbf{q})\cdot\mathbf{d}_m^{(1)}} \\ &= iK_1 + 2K_1\delta q \sin\phi_{\rm M} + O(\delta q^2) \end{aligned}$$

(where $\tan\phi_{\rm M} \equiv \delta q_y/\delta q_x$),

$$\begin{aligned} f_3(\mathbf{k}) &= -i2\zeta K_1 \sum_{m=1}^{3} e^{-i\mathbf{k}\cdot\mathbf{d}_m^{(3)}} = -i2\zeta K_1 \sum_{m=1}^{3} e^{i2\mathbf{k}\cdot\mathbf{d}_m^{(1)}} \\ &= -i2\left(\frac{1}{6}+\frac{1}{3}\eta\right) K_1 \sum_{m=1}^{3} e^{i2(\hat{\mathbf{x}}2\sqrt{3}\pi+\delta\mathbf{q})\cdot\mathbf{d}_m^{(1)}} \\ &= -i(1+2\eta)K_1 + O(\delta q^2), \end{aligned}$$

and

$$\begin{aligned} f_4(\mathbf{k}) &= -i\eta K_1 \sum_{m=1}^{6} e^{-i\mathbf{k}\cdot\mathbf{d}_m^{(4)}} \\ &= -i\eta K_1 \left[\left\{ \sum_{m=1}^{3} e^{-i\mathbf{k}\cdot\mathbf{d}_m^{(1)}} \right\} \left\{ \sum_{m=1}^{3} e^{-i2\mathbf{k}\cdot\mathbf{d}_m^{(1)}} \right\} - \sum_{m=1}^{3} e^{-i3\mathbf{k}\cdot\mathbf{d}_m^{(1)}} \right] \\ &= -i\eta K_1 \left[\left\{ \sum_{m=1}^{3} e^{-i(\hat{\mathbf{x}}2\sqrt{3}\pi+\delta\mathbf{q})\cdot\mathbf{d}_m^{(1)}} \right\} \left\{ \sum_{m=1}^{3} e^{-i2(\hat{\mathbf{x}}2\sqrt{3}\pi+\delta\mathbf{q})\cdot\mathbf{d}_m^{(1)}} \right\} - \sum_{m=1}^{3} e^{-i3(\hat{\mathbf{x}}2\sqrt{3}\pi+\delta\mathbf{q})\cdot\mathbf{d}_m^{(1)}} \right] \\ &= i2\eta K_1 + O(\delta q^2) \end{aligned}$$

put together gives

$$\begin{aligned} f(\mathbf{k}) &= f_1(\mathbf{k}) + f_3(\mathbf{k}) + f_4(\mathbf{k}) \\ &= 2K_1\delta q \sin\phi_{\rm M} + O(\delta q^2), \end{aligned}$$

while

$$\begin{aligned} M(\mathbf{k}) &= -K_2 \sum_{m=1}^{3} \sin\left[(\hat{\mathbf{x}}2\sqrt{3}\pi + \delta\mathbf{q})\cdot\mathbf{d}_m^{(2)}\right] \\ &= -2\sqrt{3}K_2\delta q\cos\phi_{\rm M} + O(\delta q^2). \end{aligned}$$

Combined, we obtain around M

$$\mathcal{F}(\mathbf{k})\cdot\boldsymbol{\sigma} = 2\delta q(-\sigma^z\sqrt{3}K_2\cos\phi_{\rm M} + \sigma^x 2K_1\sin\phi_{\rm M}) \quad \text{(E2)}$$

up to the first order. This shows how a Majorana cone can arise with the inclusion of the $M(\mathbf{k})$ contribution. There being three M points in the 1st BZ, we can conclude that three Majorana cones appear at $\zeta = \frac{1}{6} + \frac{1}{3}\eta$.

For $\mathcal{F}(\mathbf{k})$ around Γ for $\zeta = -\frac{1}{2} - \eta + \delta$ up to the third order in k and $\delta \ll k^3$,

$$f_1(\mathbf{k}) = K_1\left(-i3 + i\frac{3}{4}k^2 + \frac{1}{8}k^3\sin 3\phi\right)$$

(where $\tan\phi \equiv k_y/k_x$),

$$f_3(\mathbf{k}) = (1+2\eta-2\delta)K_1(i3 - i3k^2 + k^3\sin 3\phi),$$

and

$$f_4(\mathbf{k}) = \eta K_1\left(-i6 + i\frac{9}{2}k^2\right)$$

put together gives

$$\begin{aligned} f(\mathbf{k}) &= f_1(\mathbf{k}) + f_3(\mathbf{k}) + f_4(\mathbf{k}) \\ &= -iK_1\left[6\delta + \left(\frac{9}{4}+\frac{3}{2}\eta\right)k^2\right] \\ &\quad + \left(\frac{9}{8}+2\eta\right)K_1k^3\sin 3\phi, \end{aligned}$$

while

$$\begin{aligned} M(\mathbf{k}) &= -K_2 \sum_{m=1}^{3} \sin\left[\mathbf{k}\cdot\mathbf{d}_m^{(2)}\right] \\ &= \frac{3\sqrt{3}}{2}K_2k^3\cos 3\phi. \end{aligned}$$

Combined, we obtain around Γ

$$\begin{aligned} \mathcal{F}(\mathbf{k})\cdot\boldsymbol{\sigma} &= \frac{3\sqrt{3}}{8}k^3\left[\sigma^z 4K_2\cos 3\phi + \sigma^x\sqrt{3}\left(1+\frac{16}{9}\eta\right)K_1\sin 3\phi\right] \\ &\quad + \sigma^y K_1\left[6\delta + \frac{9}{4}\left(1+\frac{2}{3}\eta\right)k^2\right] + O(k^4). \end{aligned} \quad \text{(E3)}$$

This shows that, while we have a quadratic band touching at Γ for $\zeta = -\frac{1}{2} - \eta$, *i.e.* $\delta = 0$, there occurs a $\Delta\mathcal{C} = 3$ topological quantum phase transition as we cross $\zeta = -\frac{1}{2} - \eta$, *i.e.* δ changes its sign.

[1] A. Kitaev, Anyons in an exactly solved model and beyond, Ann. Phys. (N. Y.) **321**, 2 (2006).

[2] L. Savary and L. Balents, Quantum spin liquids: a review, Rep. Prog. Phys. **80**, 016502 (2016).

[3] Y. Zhou, K. Kanoda, and T.-K. Ng, Quantum spin liquid states, Rev. Mod. Phys. **89**, 025003 (2017).

[4] J. Knolle and R. Moessner, A field guide to spin liquids, Annu. Rev. Condens. Matter Phys. **10**, 451 (2019).

[5] C. Broholm, R. J. Cava, S. A. Kivelson, D. G. Nocera, M. R. Norman, and T. Senthil, Quantum spin liquids, Science **367**, eaay0668 (2020).

[6] G. Jackeli and G. Khaliullin, Mott Insulators in the Strong Spin-Orbit Coupling Limit: From Heisenberg to a Quantum Compass and Kitaev Models, Phys. Rev. Lett. **102**, 017205 (2009).

[7] J. Chaloupka, G. Jackeli, and G. Khaliullin, Kitaev-Heisenberg Model on a Honeycomb Lattice: Possible Exotic Phases in Iridium Oxides A_2IrO_3, Phys. Rev. Lett. **105**, 027204 (2010).

[8] S. M. Winter, A. A. Tsirlin, M. Daghofer, J. van den Brink, Y. Singh, P. Gegenwart, and R. Valentí, Models and materials for generalized Kitaev magnetism, Journal of Physics: Condensed Matter **29**, 493002 (2017).

[9] H. Takagi, T. Takayama, G. Jackeli, G. Khaliullin, and S. E. Nagler, Concept and realization of Kitaev quantum spin liquids, Nature Reviews Physics **1**, 264 (2019).

[10] Y. Motome and J. Nasu, Hunting Majorana Fermions in Kitaev Magnets, J. Phys. Soc. Jpn. **89**, 012002 (2020).

[11] Y. Matsuda, T. Shibauchi, and H.-Y. Kee, Kitaev Quantum Spin Liquids (2025), arXiv:2501.05608 [cond-mat.str-el].

[12] Y. Kasahara, T. Ohnishi, Y. Mizukami, O. Tanaka, S. Ma, K. Sugii, N. Kurita, H. Tanaka, J. Nasu, Y. Motome, T. Shibauchi, and Y. Matsuda, Majorana quantization and half-integer thermal quantum Hall effect in a Kitaev spin liquid, Nature **559**, 227 (2018).

[13] T. Yokoi, S. Ma, Y. Kasahara, S. Kasahara, T. Shibauchi, N. Kurita, H. Tanaka, J. Nasu, Y. Motome, C. Hickey, S. Trebst, and Y. Matsuda, Half-integer quantized anomalous thermal Hall effect in the Kitaev material candidate α-RuCl3, Science **373**, 568 (2021).

[14] O. Tanaka, Y. Mizukami, R. Harasawa, K. Hashimoto, K. Hwang, N. Kurita, H. Tanaka, S. Fujimoto, Y. Matsuda, E. G. Moon, and T. Shibauchi, Thermodynamic evidence for a field-angle-dependent Majorana gap in a Kitaev spin liquid, Nature Physics **18**, 429 (2022).

[15] K. Imamura, S. Suetsugu, Y. Mizukami, Y. Yoshida, K. Hashimoto, K. Ohtsuka, Y. Kasahara, N. Kurita, H. Tanaka, P. Noh, J. Nasu, E.-G. Moon, Y. Matsuda, and T. Shibauchi, Majorana-fermion origin of the planar thermal Hall effect in the Kitaev magnet α-$RuCl_3$, Science Advances **10**, eadk3539 (2024).

[16] J. G. Rau, E. K.-H. Lee, and H.-Y. Kee, Generic Spin Model for the Honeycomb Iridates beyond the Kitaev Limit, Phys. Rev. Lett. **112**, 077204 (2014).

[17] V. M. Katukuri, S. Nishimoto, V. Yushankhai, A. Stoyanova, H. Kandpal, S. Choi, R. Coldea, I. Rousochatzakis, L. Hozoi, and J. Van Den Brink, Kitaev interactions between $j = 1/2$ moments in honeycomb Na_2IrO_3 are large and ferromagnetic: insights from ab initio quantum chemistry calculations, New J. Phys. **16**, 013056 (2014).

[18] S. K. Choi, R. Coldea, A. N. Kolmogorov, T. Lancaster, I. I. Mazin, S. J. Blundell, P. G. Radaelli, Y. Singh, P. Gegenwart, K. R. Choi, S.-W. Cheong, P. J. Baker, C. Stock, and J. Taylor, Spin Waves and Revised Crystal Structure of Honeycomb Iridate Na_2IrO_3, Phys. Rev. Lett. **108**, 127204 (2012).

[19] J. A. Sears, M. Songvilay, K. W. Plumb, J. P. Clancy, Y. Qiu, Y. Zhao, D. Parshall, and Y.-J. Kim, Magnetic order in $\alpha - RuCl_3$: A honeycomb-lattice quantum magnet with strong spin-orbit coupling, Phys. Rev. B **91**, 144420 (2015).

[20] R. D. Johnson, S. C. Williams, A. A. Haghighirad, J. Singleton, V. Zapf, P. Manuel, I. I. Mazin, Y. Li, H. O. Jeschke, R. Valentí, and R. Coldea, Monoclinic crystal structure of $\alpha - RuCl_3$ and the zigzag antiferromagnetic ground state, Phys. Rev. B **92**, 235119 (2015).

[21] H.-S. Kim, V. S. V., A. Catuneanu, and H.-Y. Kee, Kitaev magnetism in honeycomb $RuCl_3$ with intermediate spin-orbit coupling, Phys. Rev. B **91**, 241110 (2015).

[22] H. B. Cao, A. Banerjee, J.-Q. Yan, C. A. Bridges, M. D. Lumsden, D. G. Mandrus, D. A. Tennant, B. C. Chakoumakos, and S. E. Nagler, Low-temperature crystal and magnetic structure of $\alpha-RuCl_3$, Phys. Rev. B **93**, 134423 (2016).

[23] S. M. Winter, Y. Li, H. O. Jeschke, and R. Valentí, Challenges in design of Kitaev materials: Magnetic interactions from competing energy scales, Phys. Rev. B **93**, 214431 (2016).

[24] J. Wang, B. Normand, and Z.-X. Liu, One Proximate Kitaev Spin Liquid in the $K-J-\Gamma$ Model on the Honeycomb Lattice, Phys. Rev. Lett. **123**, 197201 (2019).

[25] J. Wang, Q. Zhao, X. Wang, and Z.-X. Liu, Multinode quantum spin liquids on the honeycomb lattice, Phys. Rev. B **102**, 144427 (2020).

[26] L. N. Bulaevskii, C. D. Batista, M. V. Mostovoy, and D. I. Khomskii, Electronic orbital currents and polarization in Mott insulators, Phys. Rev. B **78**, 024402 (2008).

[27] S. Miyahara and N. Furukawa, Theory of antisymmetric spin-pair-dependent electric polarization in multiferroics, Phys. Rev. B **93**, 014445 (2016).

[28] A. Bolens, Theory of electronic magnetoelectric coupling in d^5 Mott insulators, Phys. Rev. B **98**, 125135 (2018).

[29] R. Chari, R. Moessner, and J. G. Rau, Magnetoelectric generation of a Majorana-Fermi surface in Kitaev's honeycomb model, Phys. Rev. B **103**, 134444 (2021).

[30] P. Noh, K. Hwang, and E.-G. Moon, Manipulating topological quantum phase transitions of Kitaev's quantum spin liquids with electric fields, Phys. Rev. B **109**, L201105 (2024).

[31] T. Koyama, Y. Nakatani, J. Ieda, and D. Chiba, Electric field control of magnetic domain wall motion via modulation of the Dzyaloshinskii-Moriya interaction, Sci. Adv. **4**, eaav0265 (2018).

[32] J. c. v. Chaloupka and G. Khaliullin, Hidden symmetries of the extended Kitaev-Heisenberg model: Implications for the honeycomb-lattice iridates A_2IrO_3, Phys. Rev. B **92**, 024413 (2015).

[33] D. Takikawa and S. Fujimoto, Impact of off-diagonal exchange interactions on the Kitaev spin-liquid state of $\alpha-RuCl_3$, Phys. Rev. B **99**, 224409 (2019).

[34] D. I. Khomskii and S. V. Streltsov, Orbital effects in

solids: Basics, recent progress, and opportunities, Chem. Rev. **121**, 2992 (2020).
[35] H. Liu, J. c. v. Chaloupka, and G. Khaliullin, Exchange interactions in d^5 Kitaev materials: From Na_2IrO_3 to $\alpha-RuCl_3$, Phys. Rev. B **105**, 214411 (2022).
[36] B. Wolf, D. A. S. Kaib, A. Razpopov, S. Biswas, K. Riedl, S. M. Winter, R. Valentí, Y. Saito, S. Hartmann, E. Vinokurova, T. Doert, A. Isaeva, G. Bastien, A. U. B. Wolter, B. Büchner, and M. Lang, Combined experimental and theoretical study of hydrostatic He-gas pressure effects in $\alpha-RuCl_3$, Phys. Rev. B **106**, 134432 (2022).
[37] X. Wang, F. Zhu, N. Qureshi, K. Beauvois, J. Song, T. Mueller, T. Brückel, and Y. Su, Hydrostatic pressure effects in the Kitaev quantum magnet α-$RuCl_3$: A single-crystal neutron diffraction study (2023), arXiv:2304.00632 [cond-mat.str-el].
[38] A. Hauspurg, S. Singh, T. Yanagisawa, V. Tsurkan, J. Wosnitza, W. Brenig, N. B. Perkins, and S. Zherlitsyn, Spin-strain interactions under hydrostatic pressure in α-$RuCl_3$ (2025), arXiv:2503.04656 [cond-mat.str-el].
[39] J. G. Rau and H.-Y. Kee, Trigonal distortion in the honeycomb iridates: Proximity of zigzag and spiral phases in Na_2IrO_3 (2014), arXiv:1408.4811 [cond-mat.str-el].
[40] F. D. M. Haldane, Model for a Quantum Hall Effect without Landau Levels: Condensed-Matter Realization of the "Parity Anomaly", Phys. Rev. Lett. **61**, 2015 (1988).
[41] K. Hwang, A. Go, J. H. Seong, T. Shibauchi, and E.-G. Moon, Identification of a Kitaev quantum spin liquid by magnetic field angle dependence, Nat. Commun. **13**, 323 (2022).
[42] D. Takikawa and S. Fujimoto, Topological phase transition to Abelian anyon phases due to off-diagonal exchange interaction in the Kitaev spin liquid state, Phys. Rev. B **102**, 174414 (2020).
[43] S.-S. Zhang, C. D. Batista, and G. B. Halász, Toward Kitaev's sixteenfold way in a honeycomb lattice model, Phys. Rev. Res. **2**, 023334 (2020).
[44] Y. Liu, K. Slagle, K. S. Burch, and J. Alicea, Dynamical Anyon Generation in Kitaev Honeycomb Non-Abelian Spin Liquids, Phys. Rev. Lett. **129**, 037201 (2022).
[45] K. Klocke, Y. Liu, G. B. Halász, and J. Alicea, Spin-liquid-based topological qubits (2024), arXiv:2411.08093 [cond-mat.str-el].
[46] J. Nasu, Majorana quasiparticles emergent in Kitaev spin liquid, Prog. Theor. Exp. Phys. **2024**, 08C104 (2023).
[47] D. Sticlet and F. Piéchon, Distant-neighbor hopping in graphene and Haldane models, Phys. Rev. B **87**, 115402 (2013).
[48] D. Sticlet, F. Piéchon, J.-N. Fuchs, P. Kalugin, and P. Simon, Geometrical engineering of a two-band Chern insulator in two dimensions with arbitrary topological index, Phys. Rev. B **85**, 165456 (2012).
[49] C. Bena and L. Simon, Dirac point metamorphosis from third-neighbor couplings in graphene and related materials, Phys. Rev. B **83**, 115404 (2011).
[50] M. Hermanns, K. O'Brien, and S. Trebst, Weyl Spin Liquids, Phys. Rev. Lett. **114**, 157202 (2015).
[51] S.-S. Zhang, Z. Wang, G. B. Halász, and C. D. Batista, Vison Crystals in an Extended Kitaev Model on the Honeycomb Lattice, Phys. Rev. Lett. **123**, 057201 (2019).
[52] N. Read and D. Green, Paired states of fermions in two dimensions with breaking of parity and time-reversal symmetries and the fractional quantum Hall effect, Phys. Rev. B **61**, 10267 (2000).
[53] S. C. Furuya and M. Sato, Electric-field control of magnetic anisotropies: Applications to Kitaev spin liquids and topological spin textures, Phys. Rev. Res. **6**, 013228 (2024).